JOURNAL OF GEOPHYSICAL RESEARCH, VOL. 112, D18204, doi:10.1029/2006JD008187, 2007

Analysis of charge transport during lightning using balloon-borne electric field sensors and Lightning Mapping Array

William W. Hager,[1] Richard G. Sonnenfeld,[2] Beyza Caliskan Aslan,[1] Gaopeng Lu,[2] William P. Winn,[2] and William L. Boeck[3]

Received 26 October 2006; revised 15 March 2007; accepted 30 May 2007; published 25 September 2007.

[1] Recently, wide band measurements of the electric field near a lightning flash have been obtained by a balloon-borne electric field sonde or Esonde. This paper develops new techniques for analyzing lightning-associated charge transport in a thundercloud by using both the Esonde data and simultaneous Lightning Mapping Array (LMA) measurements of VHF pulses emitted during lightning breakdown processes. Innovations in this paper include the following: (1) A filtering procedure is developed to separate the background field associated with instrument rotation and cloud charging processes from the lightning-induced electric field change. Because of the abrupt change in the signal caused by lightning, standard filtering techniques do not apply. A new mathematical procedure is developed to estimate the background electric field that would have existed if the lightning had not occurred. The estimated background field is subtracted from the measured field to obtain the lightning-induced field change. (2) Techniques are developed to estimate the charge transport due to lightning. At any instant of time during a cloud-to-ground (CG) flash, we estimate the charge transport by a monopole. During an intracloud (IC) flash, we estimate the charge transport by a dipole. Since the location of the monopole and dipole changes with time, they are referred to as a dynamic monopole and a dynamic dipole. The following physical constraints are used to achieve a unique fit: charge conservation during an IC flash, separation (distance between the CG monopole charge center and the ground and separation between IC dipole charge centers both exceed a minimum threshold), location (charge is placed on lightning channel), and likelihood (after a statistical analysis based on instrument uncertainty, highly unlikely charge locations are excluded). To implement the constraint that the charge is located on the lightning channel, we develop a mathematical object called the "pulse graph." Vertices in the graph are pulse locations obtained from the Lightning Mapping Array. Edges in the graph (that is, the pairs of vertices which are connected by line segments) are obtained by joining, in a systematic way, neighboring vertices. One CG and two IC flashes observed on 18 August 2004 near Langmuir Laboratory are analyzed. In the CG flash, initial strokes drained 12 C charge from an altitude of 5 km, while an intermediate stroke discharged 12 C from a higher charge center at 8 km. For the IC flashes, the current flow lagged behind the channel formation by time intervals on the order of 0.1 s, roughly the same time delay observed for lightning optical signals detected by NASA's Lightning Imaging Sensor.

Citation: Hager, W. W., R. G. Sonnenfeld, B. C. Aslan, J. Battles, G. Lu, W. P. Winn, and W. L. Boeck (2007), Analysis of charge transport during lightning using balloon-borne electric field sensors and Lightning Mapping Array, *J. Geophys. Res.*, *112*, D18204, doi:10.1029/2006JD008187.

1. Introduction

[2] *Sonnenfeld et al.* [2006] describe newly developed balloon-borne instrumentation, an Esonde, which can be used to measure thundercloud electric fields within a frequency band from 1 Hz to 5000 Hz. The goal in this earlier work was to use electric field changes in conjunction with data from the Lightning Mapping Array (LMA) to gain insight into the transport of charge by a lightning stroke. A

[1]Department of Mathematics, University of Florida, Gainesville, Florida, USA.
[2]Department of Physics and Langmuir Laboratory, New Mexico Institute of Mining and Technology, Socorro, New Mexico, USA.
[3]Computer and Information Sciences and Physics, Niagara University, Niagara University, New York, USA.

0148-0227/07/2006JD008187$09.00

detailed description of the instrument was provided as well as some preliminary modeling in which a flash was presumed to transport a charge δQ along the channel.

[3] In this paper more advanced data fitting techniques are developed. These allow us to compute the charge transport along a channel with much more detail than has been previously reported. The following new innovations are provided:

[4] 1. A new technique is developed to accurately filter the background field changes associated with instrument rotation and cloud charging processes from the field change associated with the lightning itself.

[5] 2. We introduce "constrained dynamic monopoles and dipoles" for modeling the charge transport associated with the lightning-induced electric field change. The constraints are used to reduce the infinity of possible inversions of field to charge to a single solution.

[6] In this paper we introduce our constraints, we argue for their physical plausibility, and we demonstrate the quality of fit and the level of detail that they bring out of the electric field data. These new techniques are illustrated using three flashes observed near Langmuir Laboratory in central New Mexico on 18 August 2004.

[7] For many years, ground-based measurements of the change in the electric field under a thundercloud have been used to estimate the location and amplitude of thundercloud charge distributions [*Jacobson and Krider*, 1976; *Koshak et al.*, 1999; *Koshak and Krider*, 1989, 1994; *Krehbiel et al.*, 1979; *Krehbiel*, 1981, 1986; *Murphy et al.*, 1996; *Wilson*, 1916, 1920; *Workman and Holzer*, 1939]. Recently, constraints have been incorporated in the estimation process. In particular, conservation of charge is mentioned by *Koshak and Krider* [1994] and *Koshak et al.* [1999].

[8] Five constraints on the monopole and dipole charge centers enter into our analysis: (1) In constraint C1, the charges are centered on the lightning channel. (2) In constraint C2, for a cloud-to-ground (CG) flash, the distance that charge is transported exceeds some minimal threshold Δ_{cg}. (3) In constraint C3, for a dipole, charge is conserved. (4) In constraint C4, for a dipole, the charge centers are separated by a minimal distance denoted Δ_{ic}. (5) In constraint C5, the charge centers are constrained to regions of high likelihood based on the measured fields and estimated uncertainties in the instrumentation.

[9] These constraints are described in detail throughout the paper. In C1, we constrain the charge locations to the lightning channel since it is the highway along which the charge is transported. For a CG flash, the lightning channel goes to the ground. In C2 we require that charge transported from the cloud to ground by a CG came from the cloud, not a region close to the ground. This constraint, although it may seem obvious, is needed because of the following phenomenon: The electric field at any point in space can be fit using close, large amplitude dipole charge centers. When we fit the lightning-induced electric field change by a monopole, we must take into account the image charge on the opposite side of the ground plane. Since the lightning channel for a CG reaches the ground, it may be possible to achieve a good fit to the data by placing a large amplitude monopole charge on the channel near the ground: The monopole in conjunction with the image essentially forms a dipole, which yields a good, but nonphysical match to the data. Hence, when we use a monopole to fit the lightning-induced electric field change, we require that charge center is in the cloud, not near the ground.

[10] For an intercloud or intracloud cloud (IC) flash, we require conservation of charge in C3. Also for an IC, C4 requires that the dipole charge centers satisfy a separation condition. This again prevents nonphysical fits to the data associated with close charge centers and large amplitude charge.

[11] Constraints C1–C4 are a priori constraints. We impose these constraints and search for the monopole or dipole charge configuration which best fits the electric field data. Since our measurement of the electric field contains uncertainty, the best monopole or dipole fitting the field is also uncertain. For the Esonde, one of the largest sources of error are the instrument gains, which are known to lie in certain intervals of uncertainty. For randomly chosen gains in the specified intervals of uncertainty, we compute the best estimate for the location of the monopole or dipole, subject to constraints C1–C4. An analysis of the distribution of charge center locations associated with the possible instrument gains reveals that certain locations for the charge are highly likely, while other locations are unlikely since there are a very small set of gains which are consistent with these locations. In C5 we impose additional constraints to prevent the placement of charge at these unlikely locations. C5 constraints are a posteriori constraints since they are imposed after a statistical analysis of the charge locations based on C1–C4 and the instrument uncertainty. A detailed explanation for C5 is given in section 5.

[12] To implement the constraint C1, we utilize the location of the VHF pulses generated during lightning to construct a mathematical entity which we call the pulse graph of a flash (see section 3). The use of time of arrival measurement for VHF pulses generated during lightning was pioneered by *Proctor* [1971, 1981]. The Lightning Detection and Ranging (LDAR) system deployed around the Kennedy Space Center was developed by *Lennon* [1975] based on Proctor's work. An improved LDAR system was developed by Lennon and coworkers in the early 1990s [*Maier et al.*, 1995]. In this paper we use VHF pulse location data obtained from New Mexico Tech's Lightning Mapping Array (LMA) [*Coleman et al.*, 2003; *Rison et al.*, 1999; *Thomas et al.*, 2001, 2004] which is deployed in the vicinity of Langmuir Laboratory, and which was operational during a balloon flight on 18 August 2004.

[13] LMA uses the time of arrival of VHF pulses emitted during lightning to estimate the pulse locations. The arrival times are recorded at a network of ground-based measurement stations placed around an area approximately 60 km in diameter. The delays in the arrival times at the measurement stations are used to estimate the pulse locations.

[14] VHF emission are sensitive to the sign of the associated charge since negative polarity breakdown through positive charge produces inherently stronger VHF emission than positive breakdown in negative charge regions [*Shao and Krehbiel*, 1996]. In particular, Shao and Krehbiel observed little or no radiation from the initial upward moving positive breakdown in triggered lightning. The fact that different portions of the channel are better delineated than other parts because of stronger VHF emissions is not a problem for our analysis since our charge fits

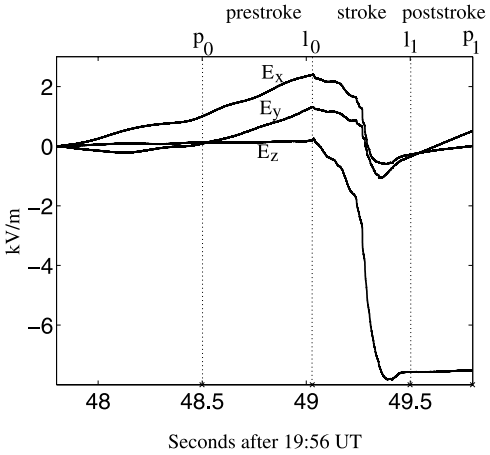

Figure 1. Three components of electric field in Earth frame of reference for IC_1, 18 August 2004, 1956 UT. The flash lies on the interval $[l_0, l_1]$ while $[p_0, l_0]$ and $[l_1, p_1]$ are prestroke and poststroke intervals used in the analysis.

utilize the channel itself, not the individual VHF pulses. Whether there are 100 pulses or a few pulses along a channel segment, we obtain approximately the same channel segment when we form the pulse graph of the flash.

[15] *Shao et al.* [1995, p. 2775] point out that detectable VHF radiation may not be generated by charge flow along already conducting channels. Again, this is not a problem for our analysis whenever the return stroke channels and channels with continuing current were made evident earlier (or later) by stepped leaders, dart leaders, or other processes. The only time we could encounter a problem with our analysis is when there were no VHF pulses at all in a part of the cloud where significant charge was deposited. If this happens, then when we try to fit the data, the fit will not be good. For the 3 flashes studied in this paper, the fits were all good, which implies that LMA delineated the regions of the cloud where significant charge was transported.

[16] As mentioned earlier, charge transport is modeled in this paper using a constrained monopole or a dipole. There are other ways of distributing charge along the lightning channel so as to match the observed electric field changes. In the work by *Sonnenfeld et al.* [2006] both a lumped and a distributed strategy are presented. In the lumped model, equal and opposite point charges are placed at systematically selected points along the channel in order to match the observed electric fields. In the distributed model, charge is placed at each LMA pulse locations, while an opposite charge is placed at the LMA initiation point. In contrast, this paper studies to what extent the observed electric fields can be fit by extremely simple models, either a monopole or a dipole.

[17] The paper is organized as follows: In section 2 we show how the electric field change associated with a flash is filtered from the background. In section 3 we introduce the pulse graph of a flash. Section 4 presents the monopole and dipole charge models and constraints C1–C4. The treatment of uncertainty in the data and C5 constraints are given in section 5, where we also analyze a CG flash of 18 August 2004. Two IC flashes of 18 August 2004, are analyzed in section 6. In section 7 we compare the relative merits of monopole versus dipole models, and we consider the importance of image charges. Section 8 gives our final conclusions.

[18] The coordinate system is defined as follows: Throughout the paper, the coordinates in plots are relative to an origin at sea level directly below a point near the NW corner of the annex building of Langmuir Laboratory. The positive x axis is directed to the east, the positive y axis points to (true) north, and the z axis is vertical, pointing away from the surface of the Earth.

2. Electric Field Change Due to Lightning

[19] Figure 1 shows an approximation to the three components of the electric field during the time of an intracloud lightning flash denoted IC_1, which began at 1956:49 UT on 18 August 2004. The coordinate system is in the Earth frame of reference. Since the Esonde measures the electric field change, the 3 plots were translated vertically so that their starting point is 0 kV/m.

[20] The nature of the approximation to the electric field can be understood from the steps used to produce Figure 1. The induced charge $Q_i(t)$, $i = 0, 1, 2, 3$, on any of the four sensing electrodes of the Esonde is transformed into the corresponding voltage $V_i(t)$ by a charge amplifier with a feedback capacitor and resistor. The equation relating charge to voltage is

$$Q_i(t) - Q_i(0) = C\left[V_i(t) + \frac{1}{RC}\int_0^t V_i(s)ds\right] - CV_i(0) := f_i(t). \tag{1}$$

[21] Here the time $t = 0$ is chosen at a convenient time before the lightning flash and f_i (t), the right-hand side of (1), is known since R and C are known and the voltage of each electrode is measured. In vector notation, we have

$$\mathbf{Q}(t) = \mathbf{f}(t) + \mathbf{Q}(0).$$

[22] The electric field $\mathbf{E}_S$ in a coordinate system that is attached to the instrument (moving relative to the Earth) is a linear function of the electrode charge $\mathbf{Q}$. In other words, there exists a time invariant 3 by 4 matrix $\mathbf{M}$ for which

$$\mathbf{E}_S(t) = \mathbf{M}\mathbf{Q}(t) = \mathbf{M}(\mathbf{f}(t) + \mathbf{Q}(0)).$$

[23] The electric field $\mathbf{E}$ in the Earth frame of reference is expressed

$$\mathbf{E}(t) = \mathbf{R}(t)\mathbf{E}_S(t) = \mathbf{R}(t)\mathbf{M}(\mathbf{f}(t) + \mathbf{Q}(0)),$$

where $\mathbf{R}(t)$ is an orthogonal matrix (rotation) associated with the orientation of the Esonde. Hence we have

$$\mathbf{R}(t)\mathbf{M}\mathbf{f}(t) = \mathbf{E}(t) - \mathbf{R}(t)\mathbf{M}\mathbf{Q}(0). \tag{2}$$

[24] Figure 1 gives the three components of $\mathbf{R}(t)\mathbf{M}\mathbf{f}(t)$; each component was translated so that it vanishes at the initial time.

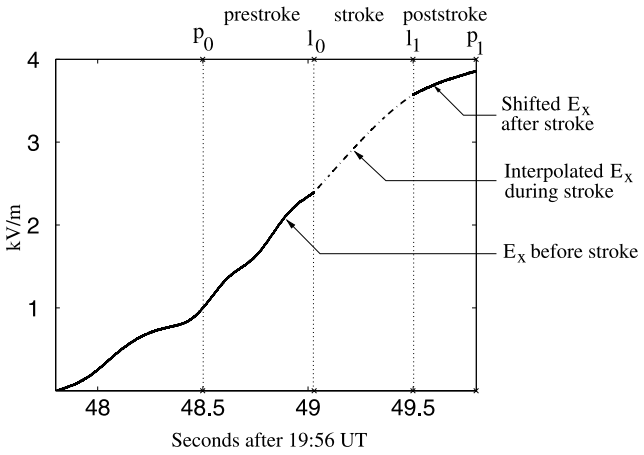

Figure 2. The x component of the background electric field $\mathbf{E}_b$ for IC_1.

[25] By (2), the measured quantity $\mathbf{R}(t)\mathbf{Mf}(t)$ is equal to the electric field in Earth frame of reference minus an unknown error term $\mathbf{R}(t)\mathbf{MQ}(0)$. The electric field itself is the sum of an abrupt electric field change $\mathbf{E}_L$ due to the lightning charge transport, and a slowly varying component $\mathbf{E}_p$ arising from charges on cloud particles. After substituting $\mathbf{E} = \mathbf{E}_L + \mathbf{E}_p$ in (2), we obtain

$$\mathbf{R}(t)\mathbf{Mf}(t) = \mathbf{E}_L(t) + \mathbf{E}_p(t) - \mathbf{R}(t)\mathbf{MQ}(0). \tag{3}$$

[26] The slowly varying parts of the electric field not arising from lightning are called the "background electric field," denoted $\mathbf{E}_b$. Referring to (3), we have

$$\mathbf{E}_b(t) = \mathbf{E}_p(t) - \mathbf{R}(t)\mathbf{MQ}(0).$$

[27] Hence (3) can be expressed

$$\mathbf{R}(t)\mathbf{Mf}(t) = \mathbf{E}_L(t) + \mathbf{E}_b(t). \tag{4}$$

[28] The lightning-induced jump in the electric field appears near the middle of Figure 1. Before the lightning at time l_0, $\mathbf{E}_L(t)$ vanishes and Figure 1 is essentially a vertically shifted $\mathbf{E}_b(t)$. After the lightning at the time labeled l_1, the plot represents the sum of $\mathbf{E}_b(t)$ and the cumulative electric field change due to the lightning. Our goal in this section is to estimate the background electric field $\mathbf{E}_b$. To obtain $\mathbf{E}_L(t)$, we subtract $\mathbf{E}_b$ from the fields plotted in Figure 1.

[29] Standard filtering techniques are not effective for separating the background electric field from the lightning-induced electric field change. The signal depicted in Figure 1 contains both a high-frequency noise, which is hidden to some degree by our thick lines, and a rapidly changing component corresponding to the lightning. Standard filtering techniques are based on the principle that the measured signal is the sum of the true signal and a disturbance which effects known Fourier components. For example, the noise in a signal is often concentrated in the high-frequency Fourier components. Hence, by discarding the high-frequency components of the Fourier analyzed signal (a low pass filter), we obtain a good approximation to the original signal without the noise. If the meaningful Fourier components are concentrated in the high frequencies, then one could discard low-frequency components (a high pass filter) to obtain the original signal.

[30] The functions shown in Figure 1 change abruptly at the time of the lightning. Essentially all the Fourier components are needed to represent such signals. If we discard the low-frequency components in an effort to remove the background, we lose on the order of 60% or more of the lightning-induced electric field signal. If we discard the high-frequency components to handle the noise, we lose a smaller fraction of the lightning electric field signal, but we are left with a signal composed of both the background (which we are trying to remove) and the lightning field change.

[31] We now describe the special filtering techniques we have developed for estimating the (slowly varying) background field. We start by partitioning the electric field record into three segments, a prestroke interval $[p_0, l_0]$, the stroke interval $[l_0, l_1]$, and the poststroke interval $[l_1, p_1]$ (see Figure 1).

[32] It is important that the stroke is contained within $[l_0, l_1]$, while the choice of p_0 and p_1 is fairly arbitrary. Currently, we choose the lightning interval by inspection of the Esonde data.

[33] Figure 2 uses the x component of the electric field of Figure 1 to show our procedure for extracting the background electric field. The left side of the graph in Figure 2 is a copy of E_x in Figure 1 up to the start of the lighting at time l_0. The right side of the graph in Figure 2, after the lightning ends at time l_1, is a shifted copy of E_x in Figure 1. The shift was chosen so that the right side of the graph is approximately an extension of the left side of the graph. In this particular case, the shift was about 4 kV/m. The shift was designed so that the left side of Figure 2 would smoothly transition with the right side of Figure 2. The dotted portion of the graph in Figure 2, between l_0 and l_1, was filled in by polynomial extrapolation. Altogether, Figure 2 represents the background electric field. We subtract the background from the measured field in Figure 1 to obtain the lightning-induced electric field change shown in Figure 3.

[34] This intuitive explanation of our techniques will now be made completely rigorous by giving precise mathemat-

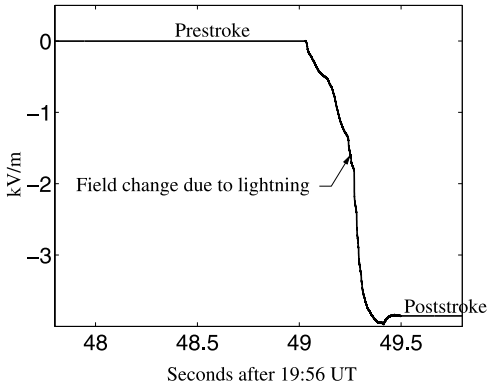

Figure 3. Electric field change due to lightning for IC_1, obtained by subtracting the background shown in Figure 2 from the original field shown in Figure 1.

ical descriptions of the three basic steps: (1) Replace prestroke and poststroke fields by polynomials. (2) Compute shift. (3) Extrapolate between prestroke and poststroke fields.

[35] To compute how much we need to shift the poststroke field so that it becomes an extension of the prestroke field, we extrapolate the prestroke field forward and we extrapolate the poststroke field backward so that they both cover the interval $[l_0, l_1]$. We choose the shift so the forward and backward extrapolated fields are as close together as possible.

2.1. Step 1 (Polynomial Fits)

[36] The prestroke and poststroke fields are fit by low degree polynomials using least squares. Mathematically, we choose the degree large enough to include the dominant terms in a Taylor expansion of the electric field. We find that second degree polynomials often yield good local fits to the slowly varying electric field components. If $\mathcal{P}_d$ denotes the set of polynomials of degree $\leq d$ and E is some component of the electric field, then the least squares fit over the prestroke time interval is the solution of the problem

$$\min_{\pi\in\mathcal{P}_d} \sum_{t\in[p_0,l_0]} (\pi(t) - E(t))^2,$$

where we typically take $d = 2$. Since $E(t)$ is known at a discrete set of times, the summation is over those measurement times $t \in [p_0, l_0]$. Let π_0 and π_1 denote the least squares polynomial fits to the field E for the intervals $[p_0, l_0]$ and $[l_1, p_1]$ respectively.

2.2. Step 2 (Computation of Shift)

[37] The shift s is chosen so that when π_0 and $s + \pi_1$ are extended over the lightning interval $[l_0, l_1]$, their extensions are as close together as possible in a least squares sense. In other words, s is the solution to the problem

$$\min_s \int_{l_0}^{l_1} (\pi_0(t) - (\pi_1(t) + s))^2 dt. \tag{5}$$

[38] Here the integration is over the time interval of the lightning. π_0 was computed using data on the interval $[p_0, l_0]$, while π_1 was computed using data on the interval $[p_1, l_1]$. When we compute s, we extend π_0 forward and π_1 backward over the interval $[l_0, l_1]$. The optimal value for s is obtained by setting to zero the derivative of the extremand in (5).

[39] From calculus we recall that the derivative of an integral is the integral of the differentiated integrand. Integrating the differentiated integrand in (5) and setting it to zero gives

$$-2\int_{l_0}^{l_1} [\pi_0(t) - (\pi_1(t) + s)]dt = 0. \tag{6}$$

[40] Since s is constant, independent of t, we have

$$\int_{l_0}^{l_1} s dt = (l_1 - l_0)s.$$

[41] Hence (6) gives

$$s = \frac{1}{l_1 - l_0}\int_{l_0}^{l_1} (\pi_0(t) - \pi_1(t))dt.$$

[42] This formula yields a shift around 4 kV/m for the right side of Figure 1.

2.3. Step 3 (Polynomial Extrapolation)

[43] Up to this point, we have generated the left and right sides of Figure 2. To complete the reconstruction of the background, we use both polynomial interpolation and a least squares process to fill in the middle part of Figure 2. Again, let E denote any component of the electric field. The polynomial π used to bridge the gap should have the following properties: (1) In property P1, π should exactly match the measured data E at time l_0, and π should exactly match the shifted data $E + s$ at time l_1. (2) In property P2, on the prestroke interval $[p_0, l_0]$, π should be close to the measured data E. (3) In property P3, on the poststroke interval $[l_1, p_1]$, π should be close to the shifted data $E + s$.

[44] Let $\bar{\pi}(t)$ denote a straight line which bridges the gap in Figure 2. This line should satisfy the two conditions $\bar{\pi}(l_0) = E(l_0)$ and $\bar{\pi}(l_1) = s + E(l_1)$. The polynomial π that we use to bridge the gap is obtained by combining the line $\bar{\pi}$ with a polynomial that vanishes at l_0 and l_1:

$$\pi(t) = \bar{\pi}(t) + (t - l_0)(t - l_1)\pi_{01}(t), \tag{7}$$

where $\pi_{01} \in \mathcal{P}_d$. The last term in (7) vanishes at $t = l_0$ and $t = l_1$ because of the factor $(t - l_0)(t - l_1)$ multiplying π_{01}. Hence π matches the line at $t = l_0$ and $t = l_1$: $\pi(l_0) = \bar{\pi}(l_0) = E(l_0)$ and $\pi(l_1) = \bar{\pi}(l_1) = E(l_1) + s$. This shows that π satisfies P1. To ensure that π is close to E on the interval $[p_0, l_0]$ and that π is close to $E + s$ on the interval $[l_1, p_1]$, we again formulate a least squares problem:

$$\min_{\pi_{01}\in\mathcal{P}_d} \left(\sum_{t\in[p_0,l_0]} (\pi(t) - E(t))^2 + \sum_{t\in[l_1,p_1]} (\pi(t) - (E(t) + s))^2 \right), \tag{8}$$

where π is given in (7). To obtain Figure 2, we took $d = 3$. As a result, π_{01} is 3rd degree and π is 5th degree. Thus, when bridging the gap between the two sides of Figure 2 we prefer polynomials of higher degree than those used for either the prestroke or poststroke intervals. This gives us greater flexibility to handle bends at the ends of the lightning interval $[l_0, l_1]$. The polynomial π is shown as a dashed curve in Figure 2. By P1, π interpolates the prestroke E_x at $t = l_0$ and the shifted poststroke E_x at $t = l_1$. The slopes at the junction points l_0 and l_1 where the polynomial joins E_x and $E_x + s$ may be discontinuous. Figure 3 shows the x component of $\mathbf{E}_L$. It is obtained by subtracting the background in Figure 2 from the measured electric field in Figure 1.

3. Pulse Graph

[45] We now consider the problem of computing the charge transfer associated with a given electric field change due to lightning. The process of inverting fields to obtain

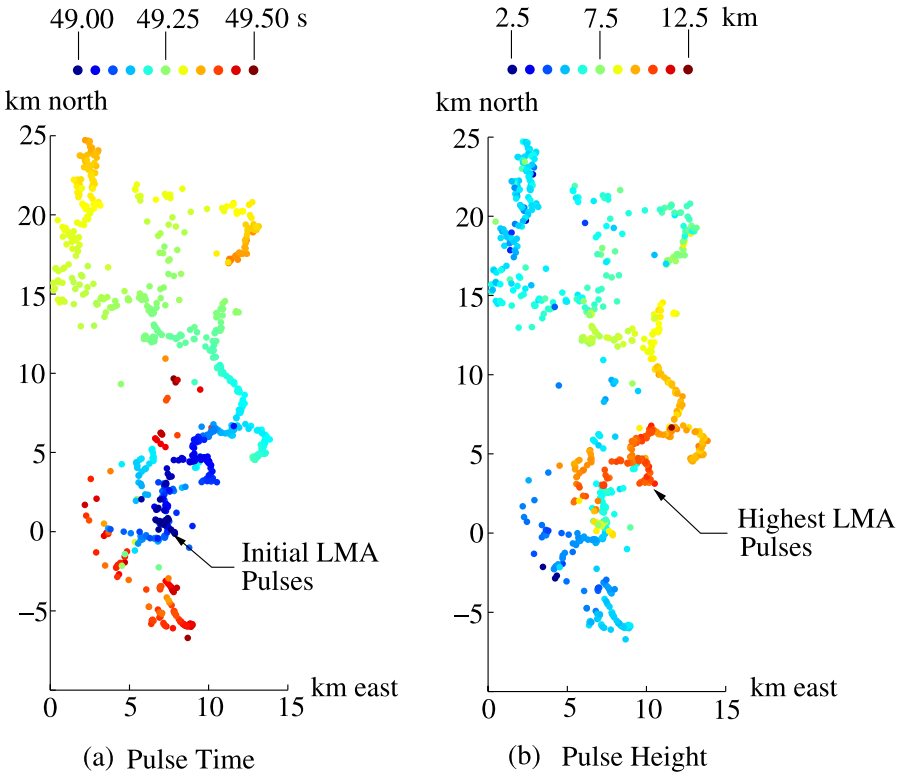

Figure 4. LMA pulses for IC_1 projected into the (x, y) plane. (a) Colors show pulse time in seconds after 1956 UT, and (b) colors show pulse height above sea level. The color scales are at the top.

charge is not unique; there are an infinite number of different charge configurations that could be used to fit a given electric field change. For example, a dipole could be placed almost anywhere in space, and with a suitable choice of the dipole charge and orientation, we could match the measured electric field. However, such a model for the charge rearrangement associated with lightning is not realistic since it is thought that lightning moves charge from one location to another location kilometers away. Moreover, the charge location is not arbitrary, it should be deposited near the lightning channel.

[46] As explained in the introduction, C1–C5 are used to reduce the infinity of possible inversions of field to charge to a unique solution. One of the most important constraints is that the charge transfer occur along the lightning channel. We use the location of VHF pulses associated with a flash to obtain a graph which approximates the lightning channel. The data used in our analysis is obtained from New Mexico Tech's Lightning Mapping Array (LMA), which is deployed in the vicinity of Langmuir Laboratory, and which was operational during the balloon flight of 18 August 2004.

[47] The LMA determines the location and time of VHF pulses produced during lightning. Figure 4a is a scatterplot for IC_1 of the projection onto the (x, y) plane of the location of VHF pulses (also called a planview). In other words, if (x_i, y_i, z_i) is the location of the ith LMA pulse, we put a dot at (x_i, y_i) in Figure 4a. The dots are colored according to the time of the pulse. The first pulse is blue while the last pulse is red. The pulses between the first and last are colored between blue and red on the basis of the relative time of the pulse, as shown in the scale at the top of Figure 4a.

[48] A complete five-panel view of IC_1 giving additional projections of the data of Figure 4 is posted on a web site for this paper: http://www.math.ufl.edu/∼hager/papers/Lightning/EsondeMarch2007.

[49] In Figure 4b we give another view of the LMA data using a planview and color based on the altitude of the pulse. The pulse with the lowest altitude is colored blue, while the pulse with the highest altitude is colored red; again, the scale is at top of Figure 4b. Comparing the LMA plots of Figure 4, we see that the VHF pulses originate in a region of intermediate altitude near (7.0, 0.0) in the (x, y) plane; they propagate to the cloud top a few kilometers to the northeast of the initiation point, and then slowly drop down to the 6 km elevation as they progress to the north. At the same time that the LMA pulses propagate northward, they also propagate to lower altitudes to the west of the initiation point. This breakdown pattern is consistent with numerical simulations of a flash [see *Hager et al.*, 1989, Figure 9] in which there are two charge centers: the initial breakdown often occurs at a point between the two charge centers, and then expands up and down connecting the two centers. Also, *Kasemir* [1960, Figure 3b] observes that for a three charge configuration with a positive charge above a negative charge above a smaller positive charge, the electric field is largest at an intermediate point between the top positive and middle negative charges. He argues that breakdown may start at this intermediate point and proceed both upward and downward.

[50] LMA generates a series of pulse locations, while the lightning channel is a curve in three dimensional space. We now explain how we generate a graph which approximates the lightning channel. A graph is a mathematical object

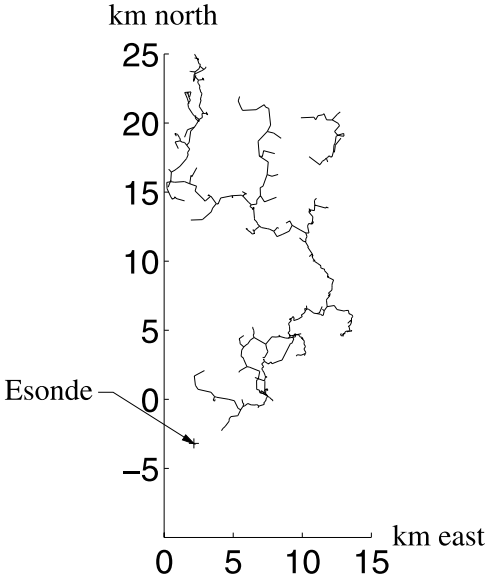

Figure 5. Pulse graph for IC_1 projected on the (x, y) plane. As indicated, the Esonde was located at roughly (2 km, −3 km) when this flash occurred.

composed of vertices and edges. Each edge in the graph is a pair of vertices which are connected by a line segment. We view the LMA pulse locations as potential vertices of the graph in three dimensional space. Since some of the LMA points may be erroneous, we first discard those pulses which are isolated from all other pulses by a distance given by a parameter "node_connect." We view these isolated LMA pulses as "LMA noise." The default value of node_connect is 1000 m, and any LMA pulse which is more than 1000 m from all other LMA pulses is discarded.

[51] We grow the channel by first connecting together neighboring nodes to form channel segments. Then channel segments are connected together when they are near other channel segments. The parameter "channel_connect" gives the maximum separation allowed when connecting neighboring channel segments. The default value for channel_connect is 2000 m; hence any channel segment separated by more than 2000 m from neighboring channel segments is left detached. Thus the graph grows through the addition of edges (or line segments), each edge is the shortest connection to a neighboring subgraph. We call the graph generated by this process the "pulse graph" of the flash.

[52] The projection onto the (x, y) plane of the pulse graph for IC_1 appears in Figure 5. Observe that the northern end of the flash contains a detached channel segment. We now explain how this detached channel segment arises. When the LMA noise was removed, a key point around (10, 20), which would have connected the detached channel to the main channel, was deleted as noise since it was separated by more than 1 km from any neighboring LMA point. After the LMA noise was discarded, the channel segment on the northern end of the flash was separated by more than 2 km from the main channel. Hence the channel segment was left detached. By playing with code parameters, it is possible to connect the detached channel segment to the main channel. For example, by increasing the parameter node_connect to 1200 m, the key LMA point near (10, 20) is retained, and the channel is no longer detached; on the other hand, some points that are clearly noise near (7, 10) are now preserved, leading to a noise polluted pulse graph. For the analysis in this paper, a stricter noise criterion works better, even though detached channel segments might occur when valid LMA points are discarded. The MATLAB code used to generate the pulse graphs appearing in this paper, PulseGraph Version 1.1, is posted on the web site for this paper (MATLAB is a registered trademark of The MathWorks, Inc.).

4. Charge Models and Location Constraints

[53] In this paper, we consider both monopole and dipole approximations to the charge transport associated with a flash. In our analysis, we approximate the Earth as a flat, perfect conductor. If the sonde is at location $\mathbf{S}$, then the measured electric field $\mathbf{E}_1$ at $\mathbf{S}$ associated with a point charge q at location $\mathbf{P}$ is given by the following formula:

$$\mathbf{E}_1 = q\mathbf{F}(\mathbf{P}),$$

where

$$\mathbf{F}(\mathbf{P}) = \frac{1}{4\pi\epsilon_0}\left(\frac{\mathbf{S}-\mathbf{P}}{||\mathbf{S}-\mathbf{P}||^3} - \frac{\mathbf{S}-\overline{\mathbf{P}}}{||\mathbf{S}-\overline{\mathbf{P}}||^3}\right).$$

[54] The constant $\frac{1}{4\pi\epsilon_0}$ has the value 9×10^9 when the electric field is in volts/meter, position is measured in meters, and the charge q is in coulombs. A bar is placed over a vector to denote its "image" value. The image of $\mathbf{P}$ is the point obtained by reflection across the plane defining the perfect conductor. For example, if the flat, perfectly conducting Earth is located at $z = 0$, then the image of $\mathbf{P} = (x, y, z)$ is $\overline{P} = (x, y, -z)$.

[55] For a dipole newly created in the sky by a lightning discharge with positive charge q at location $\mathbf{P}_-$ and (equal) negative charge $-q$ at location $\mathbf{P}_+$, the electric field $\mathbf{E}_2$ is given by

$$\mathbf{E}_2 = q(\mathbf{F}(\mathbf{P}_-) - \mathbf{F}(\mathbf{P}_+)).$$

$\mathbf{P}_-$ denotes the location where negative charge was removed from a negatively charged region of the cloud, while $\mathbf{P}_+$ is the location of the same amount of negative charge deposited by the lightning flash in the positively charged cloud region. *Krehbiel et al.* [1979] model the effect of an IC lightning discharge as the creation of a dipole. In this work, we introduce the "dynamic-dipole" in which the dipole parameters become time-dependent and are chosen to fit the time-varying electric field during the lightning discharge. Likewise, for a CG flash in which we assume that a single charge center is neutralized by the connection with ground, we introduce a "dynamic-monopole." The dynamic monopole ($\mathbf{E}_1$) and dipole ($\mathbf{E}_2$) are

$$\mathbf{E}_1(t) = q(t)\mathbf{F}(\mathbf{P}(t)) \text{ and } \mathbf{E}_2(t) = q(t)(\mathbf{F}(\mathbf{P}_-(t)) - \mathbf{F}(\mathbf{P}_+(t))). \tag{9}$$

[56] Next, we discuss the fit process and a priori constraints. In modeling an observed electric field change $\mathbf{E}_L(t)$ by a dynamic monopole or dipole $\mathbf{E}_i(t)$, $i = 1$ or 2, we

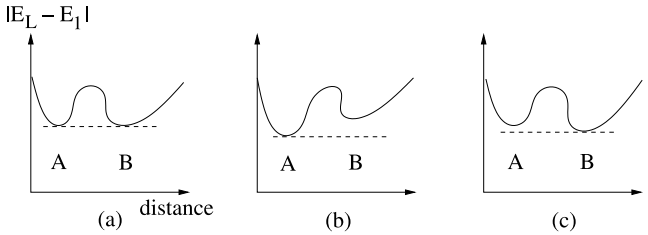

Figure 6. Schematic illustration of fit error versus location for three choices of the gains. (a) The two locations A and B have the same fit quality, (b) location A fits the data better than location B, and (c) location B fits the data better than location A.

choose the charge locations and the charge amplitude to fit the data as closely as possible in a least squares sense, subject to constraints. That is, at each instant of time where $\mathbf{E}_L(t)$ is measured, we minimize

$$||\mathbf{E}_L(t) - \mathbf{E}_1(t)|| \text{ or } ||\mathbf{E}_L(t) - \mathbf{E}_2(t)|| \text{ subject to C1} - \text{C4},$$

where $\mathbf{E}_L$ is the measured electric field and $\mathbf{E}_1$ and $\mathbf{E}_2$ are the monopole and dipole models that are fit to the measurement. The constraint C3 is built into our dipole $\mathbf{E}_2$. The constraint C1 amounts to the requirement that

$$\mathbf{P}, \mathbf{P}_-, \text{and } \mathbf{P}_+ \text{ all lie in } \mathcal{PG},$$

where $\mathcal{PG}$ denotes the pulse graph of the flash, $\mathbf{P}$ is the location of the monopole charge associated with $\mathbf{E}_1$, and $\mathbf{P}_-$ and $\mathbf{P}_+$ are the locations of the dipole charges associated with $\mathbf{E}_2$. Without the separation constraint C2, we find that a close fit to the measured fields may be achieved by putting charges near the surface of the Earth. In this case, both the charge and its image are close to one another, and close (nonphysical) data fits are achieved. In our data analysis, we take $\Delta_{cg} = 2$ km. In other words, for a CG flash we require that the charge is transported from a height at least 2 km above the surface of the Earth.

[57] Similar to the fits obtained by positioning the CG charge close to the surface of the Earth, an IC dipole with close charge centers and high charge amplitude may yield a close fit to observed electric fields. In C4 we prevent these nonphysical fits using a constraint of the form $\|\mathbf{P}_- - \mathbf{P}_+\| \geq \Delta_{ic}$. We find that Δ_{ic} should increase as the horizontal and vertical extent of the flash increases. For a flash that extends over a region of diameter D, we find that Δ_{ic} on the order of $D/2$ is large enough to prevent large amplitude, nonphysical fits to the data.

5. Uncertainty Analysis and C5 Constraints

[58] To determine the likely locations for a monopole or dipole, we perform a statistical analysis of the possible locations. The largest source of uncertainty in the Esonde's measured electric field is connected with the instrument gains G_x, G_y, and G_z described by *Sonnenfeld et al.* [2006]. As of August 2006, it is estimated that these gains lie on the following intervals:

$$2.3 \leq G_x \leq 3.1 \quad G_y = G_x, \quad 2.1 \leq G_z \leq 2.7 \qquad (10)$$

[59] For each choice of the gain within these intervals of uncertainty, we obtain a different electric field. For each electric field, we obtain a different location for the best fitting monopole or dipole (that is, the monopole or dipole which makes $\|\mathbf{E}_L - \mathbf{E}_1\|$ or $\|\mathbf{E}_L - \mathbf{E}_2\|$ as small as possible).

[60] Figure 6 depicts the rationale for the C5 constraint. The vertical axis is the fit error; the horizontal axis is the location of the monopole relative to the Esonde. The fit error may have several local minimizers as a function of distance from the Esonde. When more than one local minimizer has roughly the same fit error, then there is ambiguity in the location of the monopole. Figure 6a shows a situation where there are two local minimizers, labeled A and B, which have exactly the same fit error. Figure 6b corresponds to a different choice of the gains where the point A, closer to the Esonde than B, makes the fit error smaller. For yet another choice of the gains, the fit error resembles Figure 6c and B achieves the best fit. As we randomly choose gains in the intervals of uncertainty, we count the number of times the graph of fit error resembles Figure 6b or Figure 6c. If in 9 cases out of 10 the graph resembles Figure 6b, then we feel it is highly likely that the local minimizer closer to the Esonde provides the best estimate for the monopole location. Hence, when we compute the location of the best fitting monopole, we ignore the distant local minimizer of the fit function. In other words, we constrain our search for the best fit to a region which contains the A valley seen in Figure 6.

[61] As a concrete illustration, let us consider the CG flash of 18 August 2004, 2020 UT, described by *Sonnenfeld et al.* [2006]. The electric field, shown in Figure 7, contains 9 events which will be analyzed: The first 5 return strokes including any stepped leaders which precede them, the return stroke 6 and the continuing current which follows it, the stepped leader labeled 7, the return stroke 8, and the

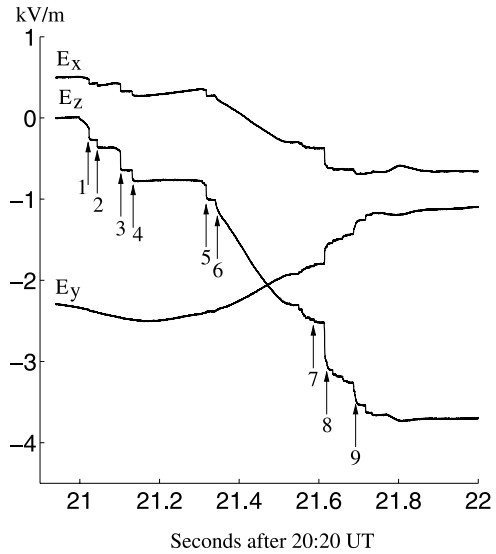

Figure 7. CG flash of 18 August 2004, 2020 UT [*Sonnenfeld et al.*, 2006], three components of electric field. Arrow 7 points to the stepped leader portion of a flash, while all the other arrows point to return strokes. Stroke 6 is followed by a continuing current which lasts about 0.2 s.

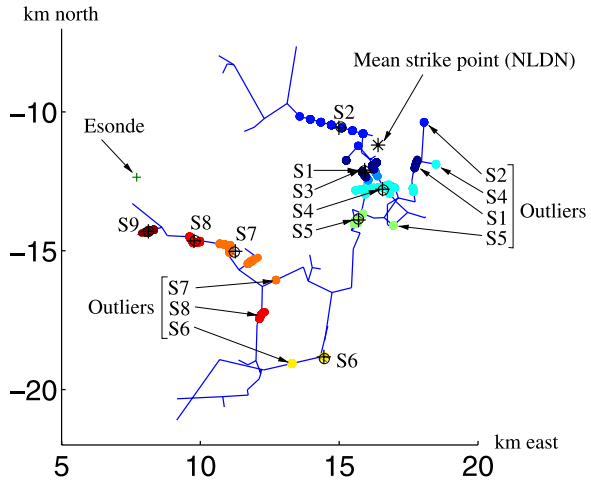

Figure 8. Monopole charge locations for 9 events in the CG flash. Different dots correspond to the locations computed using different choices of the instrument gains. Black dots show mean locations after excluding the outliers.

return stroke 9 excluding its stepped leader. Using a monopole fit, we were unable to locate the origin of the charge connected with stepped leader process preceding return stroke 9.

[62] For each choice of the gains in the intervals of uncertainty (10) and for each stroke, we obtain a different value for the field change $\mathbf{E}_L$ due to lightning. Using each value for $\mathbf{E}_L$ at the end of the stroke, we compute the best fitting monopole which satisfies constraints C1 and C2 with Δ_{cg} = 2 km. For 1000 randomly chosen gains on the intervals of uncertainty, the locations in the (x, y) plane of the best fitting monopole charge centers are shown in Figure 8, superimposed on the pulse graph for the flash. The mean strike point for the strokes reported by the National Lightning Detection Network (NLDN) is also indicated in Figure 8 (one of the strike points, which was mislocated by the NLDN, was neglected when we computed the average strike point).

[63] Observe that as different gains are selected from the intervals of uncertainty, the best fitting monopole moves between several discrete locations in Figure 8. Some of these locations are much less likely than others (labeled as outliers in Figure 8). For example, with stroke 8, there are two distinct clusters for the monopole charge. For 1000 different values of the gain, the best fitting monopole is in the southern cluster 105 times, while it is in the northern cluster 895 times. Thus for about 90% of the gains in the specified intervals of uncertainty, the best fitting monopole lies in the northern cluster. For this stroke, the fit function has two distinct local minimizers. One lies in a valley of the fit function about 4 km from the Esonde and the other lies in a valley about 8 km from the Esonde. For about 90% of the gains within the intervals of uncertainty, the closer valley is deeper, yielding a better fit to the data. For about 10% of the gains, the more distant valley gives the better fit. On the basis of this statistical analysis, we conjecture that even though the close valley does not always yield the global minimum for the fit function, the actual monopole charge is most likely located near the bottom of this valley closer to the Esonde.

[64] Hence, in the fit process we will exclude the southern region when searching for the best fitting monopole associated with stroke 8. A suitable constraint is $x \leq 11$ km. This is an example of a constraint of type C5. For each of the events, except for stroke 9, there is a cluster of points that are highly unlikely locations for the monopole charge center. By adding a simple constraint, we can exclude this location when we solve the constrained least squares problem. For event 7, the most southern cluster corresponds to only 1.9% of the gains, while for event 6, the western cluster corresponds to 22.1% of the gains. When a constraint is introduced to exclude an unlikely cluster, the global minimum is achieved in the "likely region."

[65] In Table 1, we list the C5 constraints that were introduced to exclude unlikely clusters. The last column shows the likelihood that these constraints are correct. In other words, this is the percentage of the gains for which the computed location of the charge center (the point which minimizes the fit error) satisfies the constraint.

[66] In Figure 8, the mean monopole charge locations after taking into account the C5 constraints are shown with a black dot. Since the mean location of strokes 1 and 3 are nearly the same, these two strokes extract charge from the same region in the cloud. Notice that the monopole charge locations move in a very regular manner. Stroke 2 is slightly north of stroke 1, stroke 3 coincides with stroke 1, stroke 4 is slightly south of stroke 1, stroke 5 is further south of stroke 1, stroke 6 (and its continuing current) is much further south of stroke 1. The charge origins associated with the stepped leader 7 and the return strokes 8 and 9 sweep around toward the Esonde.

[67] Detailed statistics for these 9 events are given in Table 2. The charge and location are the average over the 1000 random choices of the gains in the intervals of uncertainty (10). The relative error is the ratio $\|\mathbf{E}_L - \mathbf{E}_1\|/\|\mathbf{E}_L\|$; that is, the difference between the modeled field and the measured field divided by the measured field. The columns labeled s_x stand for the standard deviation in x.

[68] A schematic representation of the CG is given in Figure 9. There were two layers of negative charge, one at an elevation of 5 km and one at an elevation of 8 km. Strokes 1 and 3 originated from the same part of the cloud. After 12 C of negative charge was removed from the lower layer, a single stroke (and its continuing current) transported another 12 C to the ground from the upper layer. The subsequent strokes drained additional charge from the lower layer. The area of the dark circles are proportional to the charge transported by the stroke.

Table 1. C5 Constraints for the CG Flash of 18 August 2004, 2020 UT

Stroke	Constraint	Likelihood
1	$x \leq 17.0$ km	95%
2	$x \leq 17.0$ km	96%
3	$x \leq 17.0$ km	98%
4	$y \leq -12.5$ km	95%
5	$x \leq 16.5$ km	96%
6	$x \geq 14.0$ km	78%
7	$x \leq 12.5$ km	98%
8	$x \leq 11.0$ km	90%
9	no constraint	100%

Table 2. Amplitude of Charge Transport, Location, and Standard Deviations for 9 Events in a CG of 18 August 2004, 2020 UT

Stroke	q, C	s_q, C	Relative Error	X, km	Y, km	Z, km	s_X, km	s_Y, km	s_Z, km
1	3.1	0.30	0.02	15.9	−12.1	4.9	0.26	0.16	0.65
2	0.8	0.15	0.02	15.0	−10.6	5.5	0.62	0.23	0.33
3	3.4	0.22	0.03	16.0	−12.2	4.8	0.19	0.12	0.52
4	2.1	0.57	0.01	16.6	−12.8	5.4	0.72	0.10	0.79
5	2.8	0.19	0.05	15.7	−13.9	4.6	0.09	0.08	0.31
6	12.4	0.85	0.04	14.4	−18.8	8.2	0.05	0.00	0.53
7	0.7	0.17	0.03	11.3	−15.0	4.2	0.40	0.26	0.19
8	1.1	0.07	0.01	9.8	−14.6	5.0	0.15	0.08	0.27
9	0.2	0.02	0.08	8.1	−14.3	4.9	0.09	0.03	0.17

[69] Notice that event 6 is different from the other events; its amplitude is much larger and its origin is much higher in the cloud, nearly 3 km higher than the other monopole charge centers. The arrow for stroke 6 in Figure 7 is positioned at the return stroke. The stroke is followed by a continuing current which lasts on the order of 0.2 s. To investigate the possibility that stroke 6 and its continuing current may have been incorrectly located, we added a C5 constraint $z \leq 5.5$ km and recomputed the location of event 6. With this additional restriction that the monopole is located in the lower charge layer, the altitude of the best fitting charge center was 5.5 km (the imposed upper bound) and the fit error was more than 3 times the fit error for the 8 km origin. Thus the fit error is much larger when we try to force the charge origin to a lower altitude.

[70] The location of the monopole charge for event 6 in Table 2 was based on our detailed analysis of the electric field and VHF pulse locations. On the other hand, without performing any analysis, it is clear that the charge for this stroke originated from high above the Esonde. Observe that the z component of the electric field change during stroke 6 and its continuing current is much larger in magnitude than the other components of the electric field change vector. To first order, the electric field change vector during an event gives the direction of the charge origin. Because of the relatively large change in the z component of the electric field during event 6, the charge came from high above the Esonde.

[71] During event 6 there is a column of LMA pulses whose horizontal location coincides with the S6 dot in Figure 8. This column extends from the altitude 4.53 km up to 8.58 km. The pulse graph associated with this column follows the LMA pulses from 4.53 km up to 8.58 km. In the optimization, we search along this entire column (as well as all other parts of the pulse graph) seeking the best location for the monopole. As indicated in Table 2, the altitude of the best fitting monopole is 8.2 km, slightly below the highest LMA pulse in the column of pulses.

[72] In summary, the flash seems to discharge the cloud in small increments at the 5 km level, progressing between adjacent regions in the cloud. When the total charge associated with the incremental discharges reaches about 12 C, there is a single (large) discharge from the 8 km level, moving an additional 12 C of negative charge to the ground, mainly through the continuing current phase of the stroke. Balloon soundings [*Marshall and Rust*, 1991, 1993; *Stolzenburg and Marshall*, 1994; *Stolzenburg et al.*, 1994, 1998a, 1998b, 1998c, 2001, 2002] have documented that the charge in a thundercloud is layered. Since all the events except stroke 6 have charge centers at an approximate altitude of 5 km, there seems to be a negative charge layer at this altitude. There is also a layer of LMA pulses at this altitude since about half of the LMA pulses for this flash occur at altitudes between 4.5 km and 6.0 km. These LMA pulses are related to the formation and development of ionization channels along which lightning propagates toward the strike point. Since event 6 discharges 12 C from an elevation of 8 km, we conjecture that there is a second negative charge layer at this elevation. There is a column of LMA pulses associated with stroke 6 which connects the 5 km and 8 km altitudes. There are no additional LMA pulses at an altitude of 8 km. In other words, while 12 C is being drained from an altitude of 8 km by continuing currents, there is no LMA activity at this altitude, and there were only a few LMA pulses delineating the column connecting the charge layers at 5 km and 8 km elevation. Hence, in this flash there is relatively little LMA activity associated with the continuing current. This is consistent with our understanding of VHF radiation from lightning. In particular, *Shao et al*. [1995, p. 2775] state "The most basic result of radio frequency observations of lightning is that detectable VHF radiation is produced primarily by breakdown processes and not by charge flow along already conducting channels. This is not a new result but is clearly exemplified by the absence of

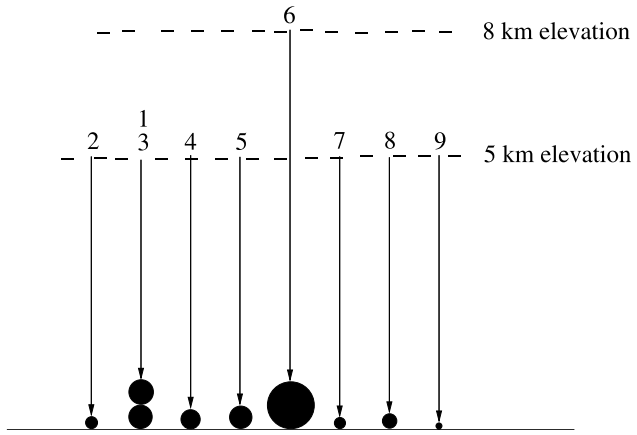

Figure 9. Sketch of the 9 events in the CG flash. Strokes 1 and 3 remove charge from the same region of the cloud. Stroke 6, with its continuing current, drains charge from a region about 3 km higher than the other strokes. The charge transport during the stepped leader 7 and the return strokes 8 and 9 are a small fraction of the charge transport during the first 6 strokes.

Table 3. Comparison of Charge Transport in This Paper (Column 2) and Its Standard Deviation (Column 3) to Charge Transport Estimates Obtained by *Sonnenfeld et al.* [2006] (Columns 4 and 5)

Stroke	q, C	s_q, C	q_{min} Prior	q_{max} Prior
1	3.1	0.30	3.5	7.0
2	0.8	0.15	1.3	2.5
3	3.4	0.22	3.5	7.0
4	2.1	0.57	1.8	3.5
5	2.8	0.19	2.0	4.0
6	12.4	0.85	5.0	15.0
7	0.7	0.17	0.2	0.6
8	1.1	0.07	2.0	6.0
9	0.2	0.02	0.5	3.0

detectable radiation during the initial parts of return strokes initiated by dart-type leaders and during large intervals of continuing current discharges to ground.''

[73] As shown in Table 2, the relative errors in the fits are quite small, while the relative errors in the charge and the location, as indicated by the standard deviations, is much larger. Since the gain errors are more than 10%, the errors in charge and location are at approximately this same level.

[74] *Sonnenfeld et al.* [2006] analyzed this CG flash using different techniques. Events 1 through 9 here correspond to strokes A through I in their work. The x and y components of $\mathbf{E}_L$ were used to predict the horizontal direction of the charge center, and the LMA was used to estimate the distance to the charge center and its height. Their height was 5 ± 1 km and the horizontal distance to the charge centers was between 2 km and 9 ± 1 km. In Table 3 we compare the charge estimates obtained using this approach (columns 4 and 5) to the estimates obtained using our constrained monopole (columns 2 and 3).

[75] Our estimates for charge transport are generally consistent with the previous estimates. Note that the constrained monopole approach computes both the charge transport and the location of the charge center. Hence, without having to manually interpret the LMA data, the optimization technique predicts that event 6 discharged from a much higher elevation than the other strokes since a point on the pulse graph at 8 km elevation fits the data much better than any other point.

[76] An interesting feature of the continuing current following return stroke 6, pointed out by a reviewer, is that there are no observable M components (perturbations or surges in the relatively steady continuing current [*Rakov and Uman*, 2003]). In rocket triggered lightning in Florida and Alabama analyzed by *Thottappillil et al.* [1995], M components have a mean duration of 2.1 ms, a mean separation of 4.9 ms, and a mean charge of 0.129 C. For a CG near the Orlando International Airport analyzed by *Mazur et al.* [1995], M events during the continuing current following the fourth stroke have durations on the order of 0.5 ms to 1 ms. For CGs in Florida analyzed by *Shao et al.* [1995], the M component durations were on the order of 0.2 ms to 1 ms. *Thottappillil et al.* [1995, p. 25,711] state that ''the M component is a necessary feature of the continuing current mode of charge transfer to ground.''

[77] Since the Esonde operates at 5000 Hz and the continuing current of event 6 transports 12 C, M components may be difficult to detect since their mean charge is on the order of 1/100 the total charge transport. Nonetheless, the larger M components reported by *Mazur et al.* [1995], *Shao et al.* [1995], or *Thottappillil et al.* [1995] might be detected, if they were present in the data. Note though that the Esonde measurements are made in the cloud, while the previously cited studies of M components were performed on the ground, possibly near the strike point of the flash if the lightning was triggered. Since our measurements, which were close to the source of the charge, do not seem to contain M components, this could imply that the source of any M components is further down the channel.

6. Intracloud Flashes

[78] In the next two subsections, we give a detailed analysis of charge transport for two intracloud flashes, the flash IC_1 introduced in section 3, and a later flash, denoted IC_2, first presented by *Sonnenfeld et al.* [2006]. The charge-transport geometry for these flashes is sketched in Figure 10. For both flashes, our analysis indicates that there is an updraft which transports positively charged hydrometeors up to an altitude of 10 to 11 km. In Figure 4, the positive updraft region coincides with the channel segment

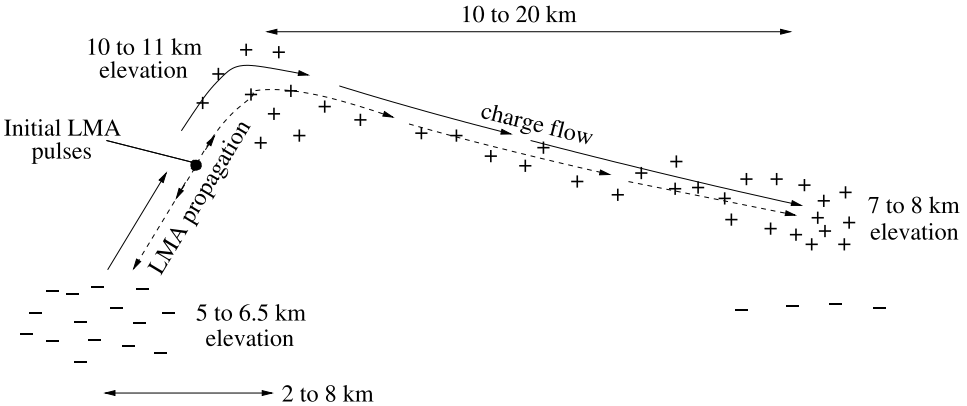

Figure 10. Sketch of the IC flashes. LMA pulses initiate at a point between the negative charge center and the positive charge center near the top of the cloud. When breakdown reaches the negative charge center, current flows to the positive charge center near the top of the cloud, and then it follows the positive charge layer which drifts down to lower altitudes.

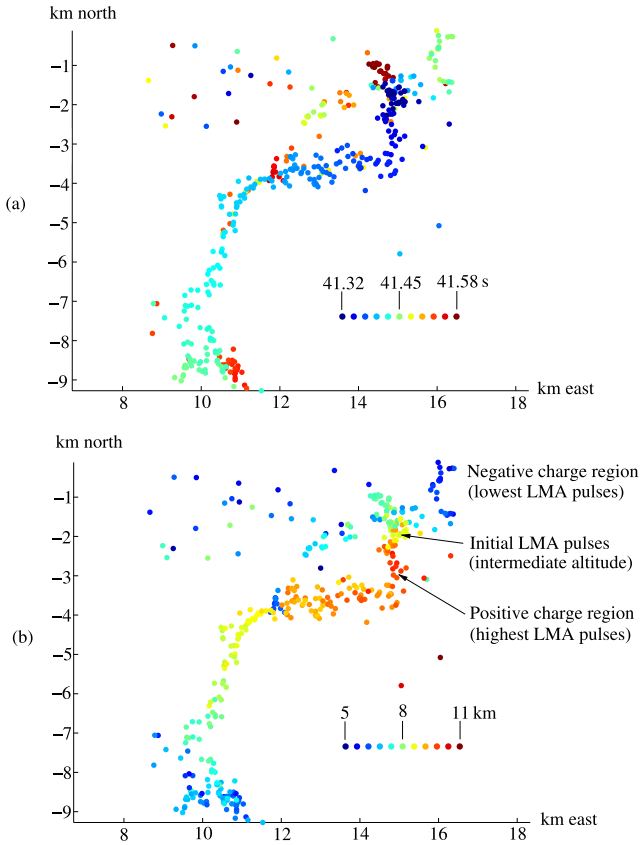

Figure 11. LMA pulses for flash IC_2. (a) Colors give time in seconds after 2012 UT, and (b) colors give height above sea level.

marked "Highest LMA Pulses." The updraft, shown schematically in Figure 10, spills to the right as the positive region drops in altitude. In Figure 4b, the drop in altitude of the upper positive layer is indicated by the evolution of colors from red to orange to yellow to green to blue as the channel progresses northward. The negative charge region is depicted on the left side of the updraft in Figure 10, at an altitude of 5 to 6.5 km. In Figure 4b, the lower negative charge center is situated on the southwest end of the channel near (5, 0). The LMA pulses initiate at a point located between the positive charge center associated with the updraft and the negative charge center. In Figure 4a, we highlight the initiation point for the LMA pulses.

[79] Our analysis will show that the lightning current follows the breakdown path from the negative charge region up to the top of the updraft, and then descends within the positive charge layer to the end of the channel. The rapid increase in charge flow along the channel occurs about the same time that the LMA pulses reach the ends of the channel, in the positive and the negative regions. During IC_1, the Esonde is positioned about 3 km from the southwest end of the channel, providing a close view of charge flow in the negatively charged region of the cloud. We observe that the dipole charge center $\mathbf{P}_-$ in the negative region starts from near the end of the channel in the negative region and moves several kilometers up the channel. During IC_2, the Esonde is positioned about 3 km from the end of the channel in the positive charge layer, giving a close view of charge flow in the positive layer. For this flash, we observe that the dipole charge center $\mathbf{P}_+$ first jumps to the top of the cloud, then reappears a few kilometers from the end of the channel in the positive layer. As charge transport continues, the dipole charge center $\mathbf{P}_+$ drifts toward the end of the channel in the positive charge layer.

[80] At the conclusion of each flash, we observed what we call "flashovers." We think of the charge transport from the negative charge center to the positive charge center and down the positive charge layer as the "normal discharge." The abnormal discharge, or flashover, occurs at the end of the flash. It is a subsequent rearrangement of charge at the end of the channel in response to the initial charge transport. In Figure 4a the flashover for IC_1 corresponds to the late LMA pulses (the red dots). These red dots, which surround the region where negative charge was drained by the flash, correspond to a local rearrangement of charge which partially replenishes the charge removed by the lightning. For IC_2, a flashover is observed at the opposite end of the channel, from a lower negative layer indicated in the right side of Figure 10 beneath the upper positive layer.

6.1. IC_2: 18 August 2004, 2012 UT

[81] In this section, we analyze an IC flash, denoted IC_2, which occurred after IC_1 at 2012 UT on 18 August 2004. A five-panel LMA plot for this flash is given by *Sonnenfeld et al.* [2006, Figure 15] as well at the web site for this paper. Plots of the LMA pulse times and heights appear in Figure 11. These plots show initial pulses at a height of 8 km to 8.5 km in the northeast center of the diagram. As mentioned already, the initial pulses are often between a positive and a negative charge center. In this case, the negative center is a few kilometers below and north of the initiation point, while the positive charge center is a few kilometers above and south of the initiation point (see Figure 11b).

[82] The mean electric field change due to lightning for IC_2, computed using the techniques of section 2, is shown in Figure 12. The mean is obtained by randomly choosing

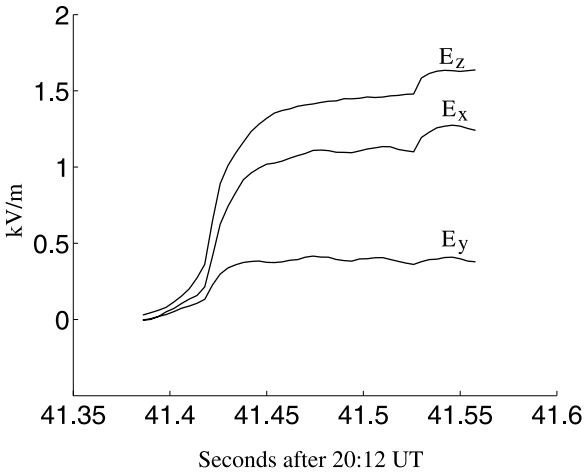

Figure 12. Lightning electric field change for IC_2 obtained by subtracting the background field from the measured field.

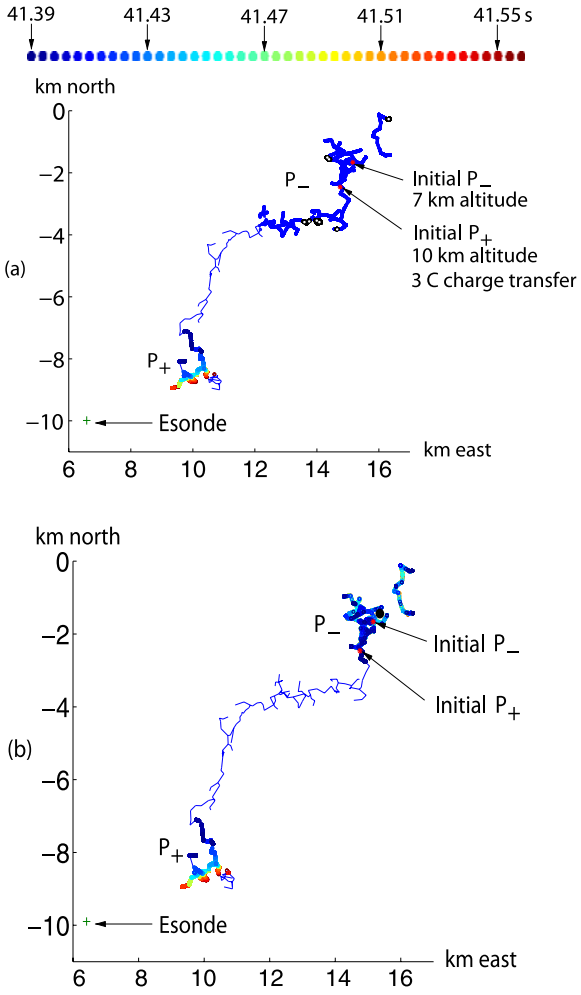

Figure 13. Location of $\mathbf{P}_-$ and $\mathbf{P}_+$ for IC_2. (a) No C5 constraints on location of $\mathbf{P}_-$ (blue), color of $\mathbf{P}_+$ based on time. The initial $\mathbf{P}_+$ and $\mathbf{P}_-$ are highlighted in the top right corner. After the initial charge transport, $\mathbf{P}_+$ moves south, beneath −7 km. Black dots correspond to 200 m by 200 m boxes with more than 1000 $\mathbf{P}_-$ points. The isolated black dot in the northeast corner contains 4764 $\mathbf{P}_-$ points, while no other box has more than 1450 points. (b) $\mathbf{P}_-$ restricted to northeast corner of flash.

500 different gains in the intervals of uncertainty and averaging the field over all the gains. It should be clarified that the fields plotted in Figure 12 are the lightning-induced fields obtained by subtracting the background from the measured fields. The measured fields are given by *Sonnenfeld et al.* [2006, Figure 14].

[83] An IC flash is best modeled by a dipole since charge is transported from one region in a thundercloud to another region. Figure 13a gives the location of the $\mathbf{P}_+$ and $\mathbf{P}_-$ charge centers for the dipole. Recall $\mathbf{P}_+$ is a point in the positive region where the negative charge is deposited and $\mathbf{P}_-$ is the source of charge in the negative region. The plot was generated in the following way: We made 500 random choices for the gains in the intervals of uncertainty (10). For each choice of the gain, we obtain a different electric field during the time interval of the flash. The flash is divided into 0.004 s time steps and for each of 48 time steps and for each of the 500 electric fields, we evaluate the best dipole fit, subject to the constraints C1, C3, and C4. The location of $\mathbf{P}_+$ for each dipole is plotted as a dot whose color is based on time, as indicated by the scale at the top of Figure 13a. The early times are blue while later times are red. The location of $\mathbf{P}_-$, which always lies north of −4 km, is plotted using blue dots.

[84] At the start of IC_2, 3 C negative charge is transferred from the negative region to the top of the positive region. The charge centers associated with this initial charge transfer to the top of the cloud are indicated by red dots in Figure 13a. Except for this initial charge transfer, the $\mathbf{P}_+$ locations are all south of $y = -7$ km. This initial charge transfer, which takes place between 41.374 s and 41.39 s after 2012 UT, corresponds to the initial small offset of E_z relative to the other components of the electric field seen in Figure 12. That is, E_z is slightly above E_x and E_y at the start of the flash since E_z grew faster (all the fields start out at 0). This offset of E_z above E_x and E_y corresponds to two charge centers located on top of each other, about 14 km from the Esonde; there is a small E_z component which dominates the other two components of the electric field. Thus, at the start of the flash, we see a small, but clear indication of the initial transfer of negative charge from a negatively charged region to the top of the cloud.

[85] After this initial charge transfer to the top of the cloud, the flash continues to propagate south and west toward the Esonde. As this charge approaches the Esonde, the measured electric field grows by an order of magnitude, and the initial dipole field is completely obscured by a new (much larger) dipole field connected with the charge transfer from the north negative region to the south positive region at the bottom of Figure 13.

[86] As seen in Figure 11b, the positive charge region drops in elevation as the flash progresses south along the channel; moreover, as seen in Figure 13a, $\mathbf{P}_+$ drifts south with time. The location of $\mathbf{P}_-$ is much more erratic than the location of $\mathbf{P}_+$. The reason that $\mathbf{P}_-$ is difficult to estimate is the following: During the second phase of the flash, $\mathbf{P}_+$ is much closer to the Esonde than $\mathbf{P}_-$. Consequently, the electric field term $\mathbf{F}(\mathbf{P}_-)$ in the dipole $\mathbf{E}_2$ is much smaller than $\mathbf{F}(\mathbf{P}_+)$. Since the $\mathbf{P}_-$ term makes a small contribution to $\mathbf{E}_2$, the computation of $\mathbf{P}_-$, the distant charge center, is relatively unstable.

[87] A single color blue is used to plot the $\mathbf{P}_-$ charge centers. The black dots with white centers indicate the regions of highest concentration of $\mathbf{P}_-$. To compute the density of $\mathbf{P}_-$ at any point, we formed boxes in the (x, y) plane of size 200 m by 200 m, and we counted the number of $\mathbf{P}_-$ points in each box. The black dots correspond to boxes with more than 1000 $\mathbf{P}_-$ points (out of the 48*500 = 24,000 possible points). The highest concentration of $\mathbf{P}_-$ occurs in the upper right corner (northeast corner). A box there has 4764 $\mathbf{P}_-$ points, while no box in any other region has more than 1450 points.

[88] In summary, for a suitable choice of the gains in the intervals of uncertainty and for a suitable sampling time, almost any point in the northeast sector of the flash could yield a best fit for $\mathbf{P}_-$. Nonetheless, in the northeast corner of the flash, there is a very small region which is a highly likely source for the charge transported by the flash. On the

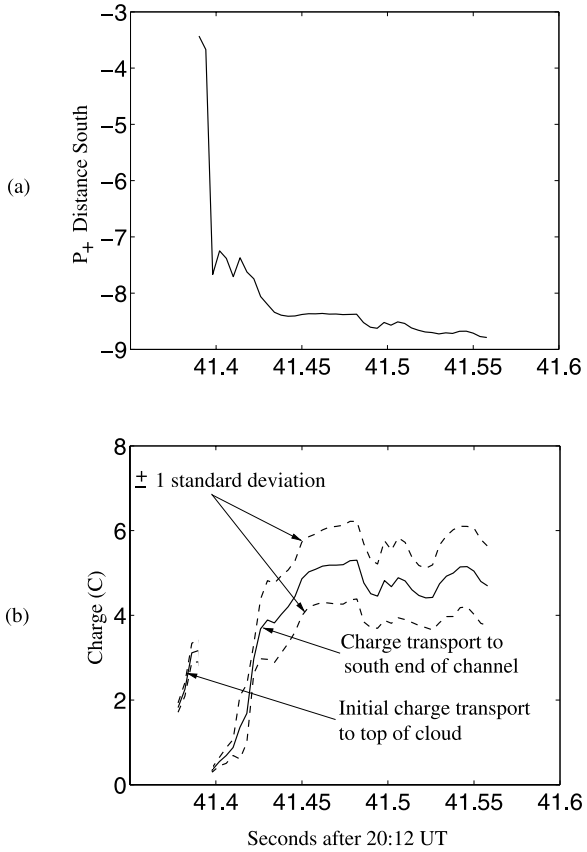

Figure 14. (a) Average y coordinate of $\mathbf{P}_+$ for IC_2. The charge moves first to the top of the cloud (the updraft was located around −3 km south) and then to the southern end of the channel. (b) Charge transport for IC_2. Initially, about 3 C is transported to the top of the cloud, and then about 5 C is transported to the southern end of the channel.

basis of this statistical analysis, we impose the following a posteriori C5 type constraint:

$$\mathbf{P}_- = \begin{bmatrix} 16.270 & \pm 2.5\text{km} \\ -0.276 & \pm 2.5\text{km} \\ 5.546 & \pm 2.5\text{km} \end{bmatrix} \tag{11}$$

[89] The centroid of this set is the specific point for which the surrounding 200 m box contains the most $\mathbf{P}_-$ points; nearly 20% of the 24,000 possible locations lie within this relatively small 200 m box. Although the set (11) has 5 km sides, $\mathbf{P}_-$ is in actually restricted to a 2.5 km box since the centroid is located on the edge of the flash. The box was chosen large enough to include the initial $\mathbf{P}_-$ indicated in Figure 13a.

[90] We now refit the data, taking into account both a priori and a posteriori constraints. Figure 13b shows that locations of the dipole charge centers. The location of $\mathbf{P}_-$ is now restricted to the upper right corner in accordance with the constraint (11). The plot is predominantly blue because of the way MATLAB generates a scatterplot; that is, points are plotted in reverse order, so that the dots at the earliest time overlay the dots at later times. If the dots were generated in their natural order, with late dots overlaying early dots, then there should be more red.

[91] Within about 0.01 s after the initial charge transfer to the top of the cloud, $\mathbf{P}_+$ reaches roughly $y = -7$ km. Figure 13b shows that as time progresses, $\mathbf{P}_+$ drifts slowly down the channel reaching $y = -8.8$ km toward the end of the flash at 2012:41.55 UT. In Figure 14a we plot the mean y coordinate of $\mathbf{P}_+$ as a function of time. Since $\mathbf{P}_+$ represents the centroid of the negative charge deposited in the positive region, perhaps half the charge has drifted past $y = -8.8$ km. In fact, in Figure 11a we see that LMA pulses are detected as far south as $y = -9.27$ km. Hence it appears that the charge is dispersed over a region that extends from $y = -7$ km to the end of the channel at $y = -9.27$ km.

[92] In Figure 14b we plot the mean charge transfer as a function of time. The mean is computed by averaging, at each sampled time, the charge transfer generated by the 500 randomly chosen gains on the intervals of uncertainty (10). The dotted lines in Figure 14b are placed 1 standard deviation above and below the mean. Figure 14b shows the two phases of the flash. In the first phase, 3 C negative charge is transferred to the top of the cloud. In the second phase, this initial charge transfer is masked by the subsequent charge transfer to the end of the channel (which is much closer to the Esonde). Figure 14b is essentially the superposition of two different figures. The first part of the graph shows the charge transfer up to the top of the cloud; in the second part of the graph, we measure the growth in charge in the southern charge center. With the available data, we cannot determine how much of the initial 3 C was left at the top of the cloud. As shown in Figure 14b, after the flash is complete, 5.1 C negative charge has been deposited at the end of the channel.

[93] In Figure 14a we see that the charge center reaches $y = -7$ km at about 41.41 s, about the same time that the LMA pulses reach this location. The LMA pulses reach the end of the channel at about 41.45 s, about the same time that most of the charge transfer is complete. The charge center does not reach the end of the channel until 41.55 s. Thus there are two distinct phases in this IC flash, an initial phase where the charge quickly propagates toward the end of the channel, stopping about 2 km from the end, and a slow phase where the charge center (and the charge) drifts toward the end of the channel.

[94] Notice that the amplitude of the charge transport depicted in Figure 14b rises and falls slightly at the end of the flash between 41.53 s and 41.55 s. This small perturbation in charge transport coincides with the small increase in the electric fields seen at 41.525 s in Figure 12 and with the late LMA pulses (red dots) observed near the bottom of Figure 11a. Referring to Figure 11b, these late LMA pulses correspond to relatively low altitude pulses (dark blue dots, 5.5 km to 6 km). This late charge movement into a region at the end of the lightning channel is the flashover introduced at the beginning of this section. At 41.525 s the transport of charge from the northeast to the southwest end of the channel is essentially complete. The fact that the fields increase after 41.525 s could indicate that charge then moved slightly closer to the Esonde, or charge increased slightly. Since the late LMA pulses are about 1 km beneath the region in the cloud where the initial 5.1 C charge had

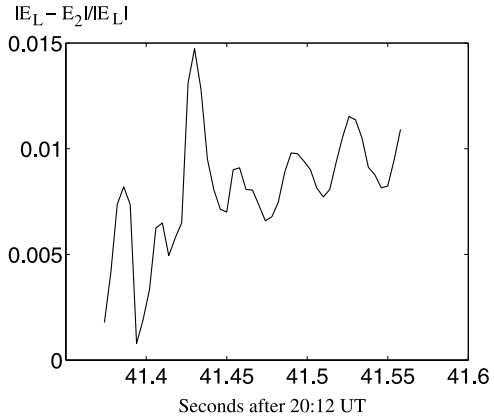

Figure 15. Average relative error in modeled electric field for IC_2. The vertical axis is obtained by subtracting the modeled electric field $\mathbf{E}_2$ from the lightning electric field change $\mathbf{E}_L$ and dividing by $\mathbf{E}_L$.

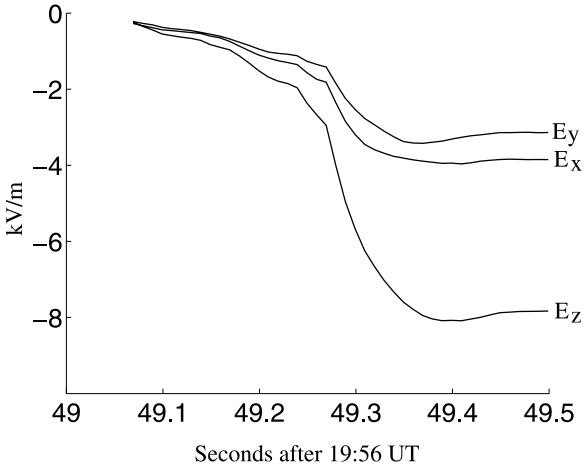

Figure 16. Lightning electric field change for IC_1 obtained by subtracting the background field from the measured field.

been deposited, there could be a lower negative layer discharging into an upper positive layer. This discharge into the positive layer moves some charge closer to the Esonde. There is no significant change in the total charge; this movement represents a local rearrangement of charge at the end of the channel in response to the initial charge transport.

[95] The relative error $\|\mathbf{E}_L - \mathbf{E}_2\|/\|\mathbf{E}_L\|$ for the fit between the measured electric field and the dynamic dipole is on the order of 1% as seen in Figure 15. Thus, for each choice of the gains in the intervals of uncertainty (10), the measured field and the modeled fields are visually identical. On the other hand, the error in the computed charges and location is much larger because of the uncertainty in the gains. In particular, the error bars for the charge transfer, indicated in Figure 14b, are on the order of 20%. Note that the relative error for the charge transfer at the start of the flash is much smaller than the relative error at the end of the flash. Even though the fields near the start of the flash are small, the computation of the initial charge centers, one above the other, was relatively stable.

6.2. IC_1: 18 August 2004, 1956 UT

[96] For a dipole with one charge center close to the Esonde and one charge center far from the Esonde, it is very difficult to estimate the location of the distant charge center since its contribution to the total dipole field $\mathbf{E}_2$ is much smaller than the contribution of the nearby charge center. For IC_2, $\mathbf{P}_+$ was about 3 km from the Esonde, while $\mathbf{P}_-$ was more than 12 km from the Esonde. Hence we obtained a better view of $\mathbf{P}_+$, while $\mathbf{P}_-$ was difficult to estimate. IC_1 has the opposite orientation, $\mathbf{P}_-$ is near the Esonde, while $\mathbf{P}_+$ may be 10 to 20 km from the Esonde. In this case, we obtain a better view of $\mathbf{P}_-$ while $\mathbf{P}_+$ is tough to estimate.

[97] In Figure 16 we plot the three components of the mean electric field change due to lightning for IC_1 corresponding to 200 randomly chosen gains in the intervals of uncertainty. In Figure 17 we show the locations of $\mathbf{P}_-$ and $\mathbf{P}_+$ obtained for the 200 randomly chosen gains and the separation parameter Δ_{ic} = 10 km. Observe that $\mathbf{P}_-$ starts about 3 km from the Esonde, near the end of the channel; as the flash progresses, $\mathbf{P}_-$ drifts about 4 km up the channel, from an initial elevation of 5000 m up to the final elevation around 6500 m. Figure 18a plots the average coordinates of $\mathbf{P}_-$ as a function of time. The computation of the distant charge center, $\mathbf{P}_+$ in this case, is much less stable. Possible locations are found throughout the upper half of Figure 17. As with IC_2, we formed 200 m boxes and counted the number of $\mathbf{P}_+$ points in each box. The box with the highest density of points is labeled in the diagram. This box contains 2,862 points, while the average location has 625 points. If the charge transfer for IC_1 is similar to the charge transfer for IC_2, then negative charge is being transported to the ends of all the channels throughout the positive region. Hence $\mathbf{P}_+$ behaves like a centroid for this

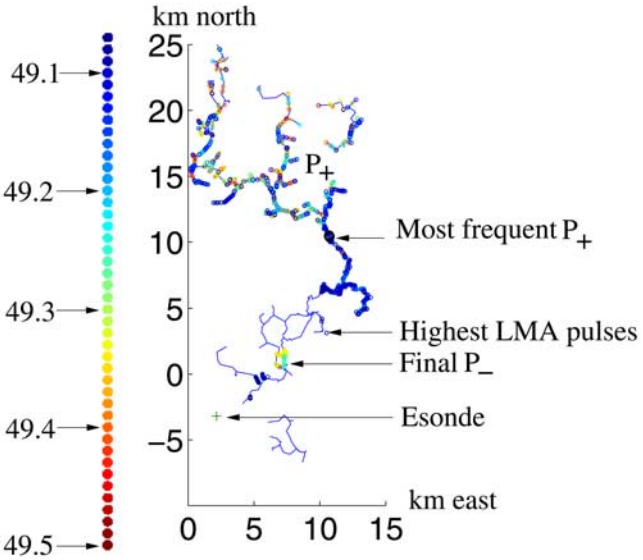

Figure 17. Location of $\mathbf{P}_-$ and $\mathbf{P}_+$ (color based on time) for IC_1. The $\mathbf{P}_-$ points are beneath $y = 3$ km, and the $\mathbf{P}_+$ points are above $y = 4$ km. The negative charge is first drained from a channel branch near the Esonde. As more charge is drained from the negative region, $\mathbf{P}_-$ moves northeast to its final location. The computation of $\mathbf{P}_+$ is relatively unstable. The most frequent $\mathbf{P}_+$ location is highlighted.

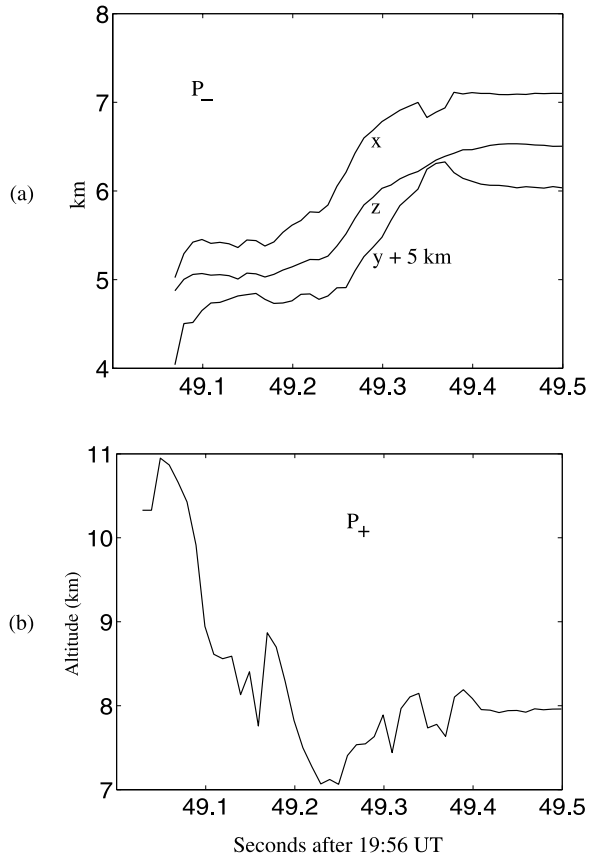

Figure 18. (a) Average coordinates of $\mathbf{P}_-$ for IC_1. The charge center drifts northeast in Figure 17, starting from a point near the Esonde and terminating at a point labeled "Final $\mathbf{P}_-$." (b) Average elevation of $\mathbf{P}_+$ for IC_1. The initial charge is transported to the top of the cloud. As time progresses, the charge center drifts northward where the positive charge layer is lower.

huge region where the charge is deposited. This interpretation of our *E* field model is consistent with the LMA plots of Figure 4. $\mathbf{P}_-$ is near the initial LMA points, whereas $\mathbf{P}_+$ is in the highly branched region which the LMA shows forming later.

[98] Although the computation of $\mathbf{P}_+$ is relatively unstable, the analysis shows that the location of $\mathbf{P}_+$ starts near the highest LMA pulses in the flash, and as time progresses, $\mathbf{P}_+$ moves to lower elevations. In Figure 18b we plot the average elevation of $\mathbf{P}_+$ as a function of time. As you can see, even the average is relatively unstable. Nonetheless, the elevation immediately reaches about 11 km and then drops to 8 km as the flash progresses. The 11 km locations correspond to the highest LMA pulses labeled in Figure 17 while the descent to lower elevations corresponds to movement along the channel segment passing through the "most frequent $\mathbf{P}_+$."

[99] In Figure 19a we see that the charge transfer for IC_1 is about 60 C, much larger than the 5.1 C transfer for IC_2. Unlike IC_2, the orientation of the Esonde relative to the positive and negative charge regions does not allow us to separate the initial charge transport to the top of the cloud from the subsequent transport down the channel. In other words, for IC_1 the charge transport from $\mathbf{P}_-$ in the negative region dominates the electric field at the Esonde. In contrast, for IC_2, there was a short initial time interval where the fields connected with both $\mathbf{P}_-$ and $\mathbf{P}_+$ were comparable, which allowed us to separate the initial and subsequent transport.

[100] In Figure 19a we see that significant charge does not start to flow until about 49.25 s after 1956 UT. This time when significant charge transport commences is also the time that LMA pulses were first detected at the end of the channel segment where $\mathbf{P}_-$ originates and at the end of the channel segment associated with the "most frequent $\mathbf{P}_+$." Moreover, the charge transport reached its peak at about 49.35 s, which is about the time that the LMA pulses reach the northern end of the flash. Hence there is almost a 0.25 s gap between the first LMA pulses and the commencement of significant charge transport. Notice that for IC_2, the rapid increase in charge flow occurs about 0.1 s after the initial LMA pulses. Thus for the smaller flash IC_2 the gap between LMA pulse initiation and rapid increase in charge flow is smaller than for IC_1. On the other hand, charge transport for IC_2 reached its peak about the same time that the LMA pulses reached the end of the channel, similar to IC_1.

[101] As with IC_2, the charge transport for IC_1 drops at the end of the flash (see Figure 19a). Referring to Figure 4, we again see that there is a flashover at the end of the flash,

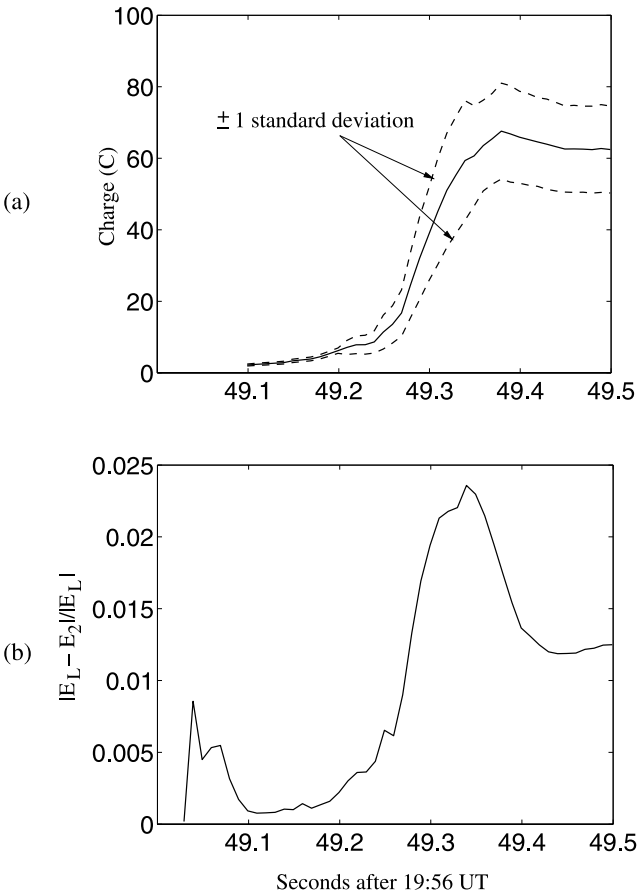

Figure 19. (a) Charge transport for IC_1. (b) Average relative error in modeled electric field for IC_1.

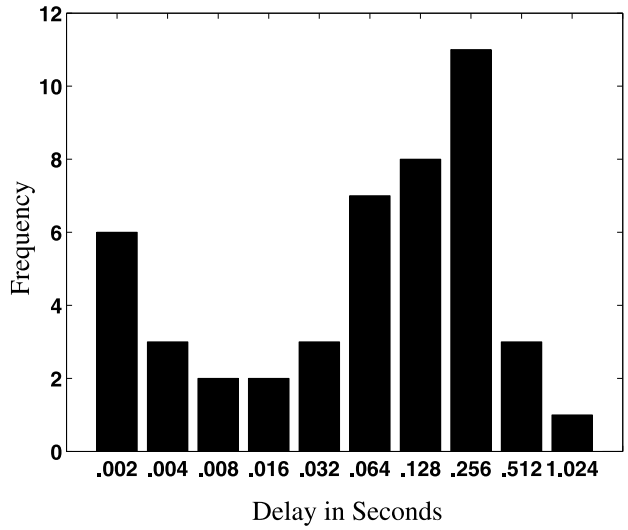

Figure 20. Delay in LIS detection of optical signal from lightning relative to initial LMA pulses. Histogram shows frequency of those delays which fall between each horizontal ordinate and its immediate predecessor on the axis.

associated with the red dots in Figure 4a. However, in this case, the flashover is from a negative charge region surrounding $\mathbf{P}_-$ into the region where 60 C has been removed by the flash. The addition of this negative charge to the region where negative charge had been removed leads to the charge drop seen in Figure 19a.

[102] The relative error $\|\mathbf{E}_L - \mathbf{E}_2\|/\|\mathbf{E}_L\|$ for the fit between the measured electric field and the dynamic dipole is on the order of 2% as seen in Figure 19b. Consequently, the dynamic dipole fit to IC_1 is not as good as the fit to IC_2. The charge in the positive region of IC_1 is spread over a much larger area than for IC_2. Hence the approximation of the charge location by a dipole constrained to the pulse graph is not as good. Nonetheless, since the negative charge center did not move by more than a few kilometers, the negative charge originates from a relatively small region, and its approximation by a single point $\mathbf{P}_-$ is reasonable. Since $\mathbf{P}_-$ is much closer to the Esonde than $\mathbf{P}_+$ and since the $\mathbf{P}_-$ term in $\mathbf{E}_2$ dominates the field, the dipole approximation to the charge transport fit the data relatively well.

7. Monopole Versus Dipole and Image Charges

[103] As we have seen with both IC_1 and IC_2, it is difficult to estimate the location of the distant charge center in a dipole approximation to the charge transport using the data from a single Esonde. An alternative approach is to neglect the distant charge center and to approximate the charge transport using a monopole. The monopole should approximate the location of the close charge center since it makes the dominant contribution to the electric field at the Esonde. For both IC_1 and IC_2 we find that a monopole approximation to the charge transport places the charge center very near the dipole charge center closest to the Esonde. The monopole approximation differs from the dipole approximation in its estimate of charge transport. For IC_1 the total charge transport for a dipole approximation was 62 C, while the monopole approximation leads to a transport of 50 C. For IC_2, the charge transport for a dipole was 5.1 C, while the monopole transport was around 4 C until the end flash (during the flashover) when the monopole charge transport jumped to 6.1 C. Generally, the monopole approximation leads to a smaller estimate for charge transport than that obtained using a dipole. In essence, the monopole approximation forms a weighted average of the distant dipole charge with the nearby dipole charge.

[104] The monopole and dipole fits $\mathbf{E}_1$ and $\mathbf{E}_2$ include both charges and their image. In cases where the terrain is uneven, it may be difficult to estimate a ground plane. To assess the importance of the image charge in the fit process, we tried to estimate the lightning-induced charge transport and location without including the image charge (equivalently, the ground plane is placed at infinity). In Figure 15, the dipole fit to IC_2 has a relative error around 1% toward the end of the flash. When we neglect the image charge, the relative error increases to 9%, and the charge transport increases to 14.8 C with a standard deviation of 17.8 C. In other words, the standard deviation in the charge transport is greater than the mean charge transport. Thus the image charge plays an important role in both monopole and dipole fits. When we neglect the image charge, we essentially cannot fit the data.

8. Conclusions

[105] Combining wide band measurements for three components of the electric field in the vicinity of a flash with GPS-synchronized LMA observations of the VHF pulses generated during lightning, we obtain estimates for the amplitude and location of the charge transported by lightning. New techniques are developed to filter the lightning induced change in the electric field from the background, and to constrain monopole and dipole fits to distinguish the actual charge transport from fictitious potential fits to the data. There were two types of constraints, a priori constraints and a posteriori constraints.

[106] The a posteriori constraints were designed to exclude unlikely locations for the charge centers based on the uncertainties in the instrumentation. One of the most important a priori constraints was that the charge centers should lie along the pulse graph, a graph whose vertices are the locations of VHF pulses generated during lightning and whose edges connect neighboring vertices. The charge change in the negative region appears to be closely approximated by a single point charge on the pulse graph. The charge which is deposited in the positive region, on the other hand, is not fit as well by a single point charge. Nonetheless, for IC_2 the negative charge is deposited in a relatively small volume in the positive region, leading to a fit error on the order of 1%. For IC_1 the negative charge deposited in the positive region is far from the Esonde; hence the error due to its approximation by a single point is relatively small.

[107] We observed an interesting delay between the formation of a channel (as indicated by initial LMA pulses) and the transport of significant charge. For IC_1, this latency was 0.25 s, while the delay for IC_2 was 0.1 s. It is not obvious from a study of the LMA data that substantial charge should not flow immediately upon creation of the channel. A similar delay has been found in the lightning generated optical signal detected by NASA's Lightning Imaging

Sensor (LIS) [see *Boeck et al.*, 2006]. In Figure 20, 46 IC flashes occurring in Oklahoma near the National Severe Storms Laboratory are analyzed. The horizontal axis shows the delay between the flash start as detected by LMA and the flash start as detected by LIS. The average delay was 0.10 s with a standard deviation of 0.13 s. Hence the delay in the charge flow as detected by the Esonde is comparable to the delay in the optical signal from lightning as detected by LIS.

[108] By utilizing Esonde electric field measurements near the source of a flash and LMA measurements of the pulses generated during lightning, we are able to infer new details concerning charge transport in both ICs and CGs, details that would be more difficult to detect using entirely ground-based instrumentation. On level ground, there is only a vertical component of the electric field, whereas at the higher altitudes of the Esonde there are three components, which can be used to gain more information about the movement of charge when used in conjunction with a Lightning Mapping Array.

[109] **Acknowledgments.** This work was funded primarily by grants 0203270, 0620286, 0619080, 0724750, and ATM-0331164 from the National Science Foundation. Additional funding was provided by the Office of the President of New Mexico Tech, by the Irving and Marion Langmuir bequest to Langmuir Laboratory, and by NASA through the New Mexico Space Grant Consortium. The field operations at Langmuir Laboratory were conducted on the Cibola National Forest under a Special Use Permit from the U.S. Forest Service. Harald Edens preprocessed the LMA data.

References

Boeck, W. L., D. M. Suszcynsky, X. Shao, R. Nemzek, H. J. Christian, S. J. Goodman, D. MacGorman, R. Thomas, and P. Krehbeil (2006), Multisensor observations of lightning in Oklahoma, *Eos. Trans. AGU*, *87*(52), Fall Meet. Suppl., Abstract AE33A-1052.

Coleman, L. M., T. C. Marshall, M. Stolzenburg, T. Hamlin, P. R. Krehbiel, W. Rison, and R. J. Thomas (2003), Effects of charge and electrostatic potential on lightning propagation, *J. Geophys. Res.*, *108*(D9), 4298, doi:10.1029/2002JD002718.

Hager, W. W., J. S. Nisbet, J. R. Kasha, and W.-C. Shann (1989), Simulations of electric fields within a thunderstorm, *J. Atmos. Sci.*, *46*, 3542–3558.

Jacobson, E. A., and E. P. Krider (1976), Electrostatic field changes produced by Florida lightning, *J. Atmos. Sci.*, *33*, 103–117.

Kasemir, H. W. (1960), A contribution to the electrostatic theory of a lightning discharge, *J. Geophys. Res.*, *65*, 1873–1878.

Koshak, W. J., and E. P. Krider (1989), Analysis of lightning field changes during active Florida thunderstorms, *J. Geophys. Res.*, *94*, 1165–1186.

Koshak, W. J., and E. P. Krider (1994), A linear method for analyzing lightning field changes, *J. Atmos. Sci.*, *51*, 473–488.

Koshak, W. J., E. P. Krider, and M. J. Murphy (1999), A multipole expansion method for analyzing lightning field changes, *J. Geophys. Res.*, *104*, 9617–9633.

Krehbiel, P. R. (1981), An analysis of the electric field change produced by lightning, Ph.D. thesis, Inst. of Sci. and Technol., Univ. of Manchester, U. K.

Krehbiel, P. R. (1986), The electrical structure of thunderstorms, in *The Earth's Electrical Environment*, pp. 90–113, National Academy Press, Washington, D. C.

Krehbiel, P. R., M. Brook, and R. A. McCrory (1979), An analysis of the charge structure of lightning discharges to ground, *J. Geophys. Res.*, *84*, 2432–2456.

Lennon, C. L. (1975), LDAR: New lightning detection and ranging system, *Eos Trans. AGU*, *56*, 991.

Maier, L., C. Lennon, T. Britt, and S. Schaefer (1995), LDAR system performance and analysis, paper presented at the 6th Conference on Aviation Weather Systems, Am. Meteorol. Soc., Boston, Mass.

Marshall, T. C., and W. D. Rust (1991), Electric field soundings through thunderstorms, *J. Geophys. Res.*, *96*, 22,297–22,306.

Marshall, T. C., and W. D. Rust (1993), Two types of vertical electrical structures in stratiform precipitation regions of mesoscale convective systems, *Bull. Am. Meteorol. Soc.*, *74*, 2159–2170.

Mazur, V., P. R. Krehbiel, and X.-M. Shao (1995), Correlated high-speed video and radio interferometric observations of a cloud-to-ground lightning flash, *J. Geophys. Res.*, *100*, 25,731–25,753.

Murphy, M. J., E. P. Krider, and M. W. Maier (1996), Lightning charge analyses in small Convection and Precipitation Electrification (CaPE) experiment storms, *J. Geophys. Res.*, *101*, 29,615–29,626.

Proctor, D. E. (1971), A hyperbolic system for obtaining VHF radio pictures of lightning, *J. Geophys. Res.*, *76*, 1478–1489.

Proctor, D. E. (1981), VHF radio pictures of cloud flashes, *J. Geophys. Res.*, *86*, 4041–4071.

Rakov, V. A., and M. A. Uman (2003), *Lightning Physics and Effects*, Cambridge Univ. Press, New York.

Rison, W., R. J. Thomas, P. R. Krehbiel, T. Hamlin, and J. Harlin (1999), A GPS-based three-dimensional lightning mapping system: Initial observations in central New Mexico, *Geophys. Res. Lett.*, *26*, 3573–3576.

Shao, X. M., and P. R. Krehbiel (1996), The spatial and temporal development of intracloud lightning, *J. Geophys. Res.*, *101*, 26,641–26,668.

Shao, X. M., P. R. Krehbiel, R. J. Thomas, and W. Rison (1995), Radio interferometric observations of cloud-to-ground lightning phenomena in Florida, *J. Geophys. Res.*, *100*, 2749–2783.

Sonnenfeld, R. G., J. D. Battles, G. Lu, and W. P. Winn (2006), Comparing E field changes aloft to lightning mapping data, *J. Geophys. Res.*, *111*, D20209, doi:10.1029/2006JD007242.

Stolzenburg, M., and T. C. Marshall (1994), Testing models of thunderstorm charge distributions with Coulomb's law, *J. Geophys. Res.*, *99*, 25,921–25,932.

Stolzenburg, M., T. C. Marshall, W. D. Rust, and B. F. Smull (1994), Horizontal distribution of electrical and meteorological conditions across the stratiform region of a mesoscale convective system, *Mon. Weather Rev.*, *122*, 1777–1797.

Stolzenburg, M., W. D. Rust, and T. C. Marshall (1998a), Electrical structure in thunderstorm convective regions: 2. Isolated storms, *J. Geophys. Res.*, *103*, 14,079–14,096.

Stolzenburg, M., W. D. Rust, and T. C. Marshall (1998b), Electrical structure in thunderstorm convective regions: 3. Synthesis, *J. Geophys. Res.*, *103*, 14,097–14,108.

Stolzenburg, M., W. D. Rust, B. F. Smull, and T. C. Marshall (1998c), Electrical structure in thunderstorm convective regions: 1. Mesoscale convective systems, *J. Geophys. Res.*, *103*, 14,059–14,078.

Stolzenburg, M., T. C. Marshall, and W. D. Rust (2001), Serial soundings of electric field through a mesoscale convective system, *J. Geophys. Res.*, *106*, 12,371–12,380.

Stolzenburg, M., T. C. Marshall, W. D. Rust, and D. L. Bartels (2002), Two simultaneous charge structures in thunderstorm convection, *J. Geophys. Res.*, *107*(D18), 4352, doi:10.1029/2001JD000904.

Thomas, R. J., P. R. Krehbiel, W. Rison, T. Hamlin, J. Harlin, and D. Shown (2001), Observations of VHF source powers radiated by lightning, *Geophys. Res. Lett.*, *28*, 143–146.

Thomas, R. J., P. R. Krehbiel, W. Rison, S. J. Hunyady, W. P. Winn, T. Hamlin, and J. Harlin (2004), Accuracy of the Lightning Mapping Array, *J. Geophys. Res.*, *109*, D14207, doi:10.1029/2004JD004549.

Thottappillil, R., J. D. Goldberg, V. A. Rakov, and M. A. Uman (1995), Properties of M components from currents measured at triggered lightning channel base, *J. Geophys. Res.*, *100*, 25,711–25,720.

Wilson, C. T. R. (1916), On some determinations of the sign and magnitude of electric discharges in lightning flashes, *Proc. R. Soc. London, Ser. A*, *92*, 555–574.

Wilson, C. T. R., III (1920), Investigations on lightning discharges and on the electric field of thunderstorms, *Philos. Trans. R. Soc. London, Ser. A*, *221*, 73–115.

Workman, E. J., and R. E. Holzer (1939), Quantities of charge transfers in lightning discharges, *Phys. Rev.*, *55*, 598.

B. C. Aslan and W. W. Hager, Department of Mathematics, University of Florida, P.O. Box 118105, Gainesville, FL 32611, USA. (hager@math.ufl.edu)

W. L. Boeck, Computer and Information Sciences and Physics, Niagara University, Niagara University, NY 14109, USA.

G. Lu, R. G. Sonnenfeld, and W. P. Winn, Department of Physics, New Mexico Institute of Mining and Technology, Socorro, NM 87801, USA.